A Fourier-space four-field resonant response model for tokamak plasmas with applications to pedestal physics

R. Fitzpatrick ●* and Y. Lin

*Institute for Fusion Studies, Department of Physics,
University of Texas at Austin, Austin TX 78712, USA*

Abstract

It is demonstrated that the two-fluid, drift-magnetohydrodynamical response of a resonant layer in a tokamak plasma to an externally generated, static, resonant magnetic perturbation (RMP) can be reduced to four, coupled, first-order, ordinary differential equations in Fourier space. It is also shown that these four equations can be conveniently solved by means of a Riccati transformation. The resulting Fourier-space, four-field, resonant plasma response model is successfully benchmarked against the equivalent configuration-space model of Lee et alia [Nucl. Fusion **64**, 106058 (2024)]. The Fourier-space model is used to estimate the response of an ITER pedestal to an RMP. The strong magnetic shear present just inside the magnetic separatrix is found to suppress the response of the plasma to the RMP to such an extent it is indistinguishable from that of a vacuum. Consequently, rational surfaces that lie in the strong-shear region can be neglected when calculating the response of the plasma to the RMP. This implies that it is not necessary to include an infinite number of rational surfaces in the calculation, despite the fact that the safety-factor asymptotes to infinity as the magnetic separatrix is approached. Furthermore, the vacuum response of the plasma in the strong-shear region is associated with the density pump-out phenomenon. The shielding of driven magnetic reconnection by the plasma is found to also break down at rational surfaces associated with comparatively low poloidal mode numbers that are situated close to the top of the pedestal. This breakdown is associated with the RMP-induced suppression of edge-localized modes.

1 Introduction

1.1 Resonant magnetic perturbations

Externally generated, static (i.e., non-rotating in the laboratory frame), *resonant magnetic perturbations* (RMPs) can drive magnetic reconnection in tokamak plasmas that are intrinsically stable to tearing modes [1, 2, 3, 4, 5]. Static RMPs arise naturally as a consequence of magnetic field-coil misalignments [6], but are sometimes deliberately applied to tokamak plasmas in order to suppress edge-localized modes (ELMs) [7]. Driven reconnection is significant because it leads to the formation of magnetic island chains at so-called *rational* magnetic flux-surfaces within the plasma [8]. Such chains locally flatten the pressure profile, and, thereby, degrade the plasma energy confinement [9].

The analysis of the response of a tokamak plasma to an RMP is most efficiently formulated as an asymptotic matching problem in which the plasma is divided into two distinct regions [10]. In the so-called *outer region*, which comprises most of the plasma, the plasma perturbation is governed by the equations of linearized, marginally-stable, ideal magnetohydrodynamics (MHD). However, these equations become singular on rational magnetic flux-surfaces at which the perturbed magnetic field resonates with the equilibrium field. In the *inner region*, which consists of a set of narrow layers centered on the various rational surfaces, non-ideal-MHD effects become important.

---

*rfitzp@utexas.edu

1.2 Four-field resonant response model

It is well known that single-fluid resistive-MHD offers a very poor description of the response of the inner region to the magnetic perturbation in the outer region. For instance, the strong diamagnetic flows present in tokamak plasmas imply that the electron and ion fluid velocities are significantly different from one another, necessitating a two-fluid drift-MHD treatment [11]. Moreover, single-fluid resistive-MHD does not take into account the important ion sound-radius lengthscale below which electron and ion dynamics become decoupled from one another [12, 13]. Previously, Cole & Fitzpatrick [14] used the four-field model of Fitzpatrick & Waelbroeck [15], which consists of four coupled nonlinear partial differential equations, and which is based on the original four-field model of Hazeltine, Kotschenreuther & Morrison [16], to determine the linear two-fluid response of a resonant layer to the perturbation in the outer region. This treatment was extended in Ref. [17] in order to take into account the anomalously large perpendicular energy diffusivity present in tokamak plasmas.

In configuration space, the four-field models of Refs. [14] and [17] yield a set of resonant layer equations that can be expressed as *ten*, coupled, first-order, linear ordinary differential equations (o.d.e.s) [18]. However, in Fourier space, the resonant layer equations can be written as *four*, coupled, first-order linear o.d.e.s [14]. It is clearly advantageous to solve the equations in Fourier space. In Refs. [14] and [17], an approximation is made by which one of the terms in the Fourier-transformed layer equations is neglected. This approximation, which is valid in low-β plasmas, is such that the layer equation that governs the parallel ion dynamics decouples from the other three equations, effectively converting a four-field resonant response model into a three-field model. Furthermore, the three remaining layer equations can be combined to give a single, second-order, linear o.d.e. This second-order equation is most conveniently solved by means of a Riccati transformation that converts it into a first-order, nonlinear o.d.e. [19, 20, 21]. The advantage of the Riccati approach is that it can deal with numerically problematic solutions that blow up as $\exp(p^2)$, or faster, at large p, where p is the Fourier transform variable.

Lee, Park & Na [18] recently demonstrated how to solve the full, tenth-order, four-field, resonant layer equations in configuration space using a Riccati transformation. In the process, they discovered that, in a high-β plasma, the RMP rotation frequency (as seen in the local $\mathbf{E} \times \mathbf{B}$ frame at the rational surface) at which the electromagnetic torque exerted on the plasma in the immediate vicinity of the resonant layer passes through zero is shifted in the ion diamagnetic direction from the electron diamagnetic frequency. This result is significant because there is some experimental evidence for such a shift [22, 23, 24].

The first aim of this paper is to demonstrate how the calculation of Lee et alia can be reimplemented in Fourier space. The Fourier version of the calculation is more convenient, from a numerical point of view, because it involves the solution of a fourth-order, rather than a tenth-order, system of equations.

1.3 Magnetically diverted plasmas

The safety-factor profile of a magnetically diverted tokamak plasma diverges logarithmically as the magnetic separatrix (a.k.a. the last closed magnetic flux-surface) is approached. At first sight, this suggests that, when determining the response of such a plasma to an RMP with a given toroidal mode number, it is necessary to include an infinite number of rational magnetic flux-surfaces in the calculation, the majority of which lie very close to the separatrix. In fact, as was demonstrated in Ref. [25], when finite plasma resistivity is taken into account, this turns out not to be the case. Instead, it is only necessary to include rational surfaces that lie in the region $0 < \Psi_N < 1 - \epsilon_c$, where Ψ_N is the normalized poloidal magnetic flux, and $0 < \epsilon_c \ll 1$. Moreover, the value of ϵ_c can be calculated from the plasma parameters at the edge of the discharge.

The analysis of Ref. [25] is based on the three-field, resonant response model of Refs. [14] and [17]. The second aim of this paper is to generalize this analysis by employing the new Fourier-space, four-field, resonant plasma response model. In particular, we wish to estimate the response of an ITER pedestal to an RMP.

1.4 Organization

This paper is organized as follows. The asymptotic matching approach to determining the response of a tokamak plasma to an RMP is described in Sect. 2. In Sect. 3, the Fourier-space, four-field, resonant plasma

response model is outlined, and benchmarked against the configuration-space model of Ref. [18]. The former model is described in detail in Appendix A. In Sect. 4, the Fourier-space, four-field, resonant plasma response model is used to estimate the response of the ITER pedestal to an RMP. Finally, the paper is summarized in Sect. 5.

2 Asymptotic matching

2.1 Plasma equilibrium

Consider a large-aspect-ratio tokamak plasma equilibrium whose magnetic flux-surfaces map out (almost) concentric circles in the poloidal plane. Such an equilibrium can be approximated as a periodic cylinder [4]. Let r, θ, z be right-handed cylindrical coordinates. The magnetic axis corresponds to $r = 0$, and the plasma boundary to $r = a$, where a is the simulated minor radius of the plasma. The system is assumed to be periodic in the z-direction with periodicity length $2\pi R_0$, where R_0 is the simulated major radius of the plasma. The safety-factor profile takes the form $q(r) = r\,B_z/[R_0\,B_\theta(r)]$, where B_z is the constant "toroidal" magnetic field-strength, and $B_\theta(r)$ is the poloidal magnetic field-strength. The equilibrium poloidal and toroidal magnetic fluxes (divided by 2π) are written $\psi_p(r) = B_z \int_0^r dr'\, r'/q(r')$ and $\psi_t(r) = B_z\, r^2/2$, respectively. The standard large aspect-ratio tokamak orderings, $r/R_0 \ll 1$ and $B_\theta/B_z \ll 1$, are adopted [21].

2.2 Outer region

Consider an externally generated, static (in the laboratory frame) magnetic perturbation that has m periods in the poloidal direction, and n periods in the toroidal direction. The response of the plasma to the perturbation is governed by the linearized equations of marginally-stable ideal-MHD everywhere in the plasma, apart from a (radially) narrow layer centered on the rational surface whose minor radius, r_s, is such that $q(r_s) = m/n$ [10].

The perturbed magnetic field is written $\delta\mathbf{B} \simeq \nabla\delta\psi \times \mathbf{e}_z$, where $\delta\psi(r, \theta, \varphi) = \delta\psi(r)\,\exp[\mathrm{i}\,(m\,\theta - n\,\varphi)]$, and $\varphi = z/R_0$ is a simulated toroidal angle. In the outer region (i.e., everywhere in the plasma apart from the resonant layer), the perturbed helical magnetic flux, $\delta\psi(r)$, satisfies the *cylindrical tearing mode equation* [21, 26, 27],

$$\frac{d^2\delta\psi}{dr^2} + \frac{1}{r}\frac{d\delta\psi}{dr} - \frac{m^2}{r^2}\,\delta\psi - \frac{J_z'\,\delta\psi}{r\,(1/q - n/m)} = 0, \tag{1}$$

where $J_z(r) = R_0\,\mu_0\,j_z(r)/B_z$, and $j_z(r)$ is the equilibrium "toroidal" current density. Here, $' \equiv d/dr$.

In general, the solution of Eq. (1) that satisfies physical boundary conditions at the magnetic axis and the plasma boundary is such that $\delta\psi(r)$ is continuous across the rational surface, whereas $d\delta\psi/dr$ is discontinuous. The discontinuity of $d\delta\psi/dr$ across the rational surface is indicative of the presence of a helical current sheet at the surface. The complex quantity $\Psi_s = \delta\psi(r_s)$ determines the amplitude and phase of the reconnected helical magnetic flux at the rational surface, whereas the complex quantity

$$\Delta\Psi_s = \left[r\,\frac{d\delta\psi}{dr}\right]_{r_{s-}}^{r_{s+}} \tag{2}$$

parameterizes the amplitude and phase of the helical current sheet [4].

The solution of the cylindrical tearing mode equation in the outer region, in the presence the RMP, leads to a *tearing mode dispersion relation* of the form [4, 10]

$$\Delta\Psi_s - E_{ss}\,\Psi_s = -E_{ss}\,\Psi_v, \tag{3}$$

where E_{ss} is a real dimensionless quantity known as the *tearing stability index* [10]. Moreover, Ψ_v is the so-called *vacuum flux*, and is defined as the reconnected magnetic flux that would be driven at the rational surface by the RMP were the plasma intrinsically tearing-stable (i.e., $E_{ss} < 0$), and were there no current sheet at the rational surface (i.e., $\Delta\Psi_s = 0$) [4].

Regime	Q_e	Q_i	c_β	D	P_E	P_φ
HRi	1.0	−1.0	1.0	10.0	1.0	$1.0 \times 10^{+0}$
HRii	1.0	−1.0	1.0	10.0	1.0	1.0×10^{-1}
RIii	0.15	−0.15	1.0	1.0	1.0	1.0×10^{-4}
VRii	0.15	−0.15	1.0	0.1	1.0	$1.0 \times 10^{+0}$

Table 1: The normalized layer parameters used in the benchmark comparisons shown in Figs. 1–4.

In the following, it is assumed that $E_{ss} < 0$, which implies that the tearing mode that reconnects magnetic flux at the rational surface is intrinsically stable. In this case, any magnetic reconnection that takes place at the surface is entirely due to the RMP.

2.3   Inner region

The current sheet at the rational surface is resolved by employing a two-fluid, drift-MHD, resonant response model in the inner region (i.e., the region of the plasma in the immediate vicinity of the rational surface) to determine the complex *layer response index*, Δ_s. Asymptotic matching between the solutions in the inner and the outer regions yields

$$\Delta_s = \frac{\Delta \varPsi_s}{\varPsi_s}. \tag{4}$$

The previous two equations lead to the *layer response equation*,

$$\varPsi_s = \frac{\varPsi_v}{1 + \Delta_s/(-E_{ss})}. \tag{5}$$

Note that if $|\Delta_s|/(-E_{ss}) \ll 1$ then $\varPsi_s \simeq \varPsi_v$ and $\Delta \varPsi_s \simeq 0$, which is termed a *vacuum response*. On the other hand, if $|\Delta_s|/(-E_{ss}) \gg 1$ then $|\varPsi_s| \ll |\varPsi_v|$, which is termed an *ideal response*. In the vacuum response regime, the current sheet that is excited in the resonant layer is too feeble to prevent driven magnetic reconnection, and the reconnected flux at the rational surface is the same as that which would be driven if there were no plasma present at the surface. On the other hand, in the ideal response regime, the current sheet excited in the layer is large enough to almost completely suppress driven magnetic reconnection, which implies that the response of the plasma is equivalent to that which would occur if the ideal-MHD flux freezing constraint, $\varPsi_s = 0$, were imposed at the rational surface [25].

3   Fourier-space four-field resonant response model

3.1   Introduction

The Fourier-space, four-field, resonant plasma model employed in this paper is described in detail in Appendix A.

3.2   Dimensionless parameters

All four-field resonant response models are defined by the following seven dimensionless parameters: $Q_E = -S^{1/3} n \omega_E \tau_H$, $Q_e = -S^{1/3} n \omega_{*e} \tau_H$, $Q_i = -S^{1/3} n \omega_{*i} \tau_H$, $c_\beta = \sqrt{\beta/(1+\beta)}$, $D = S^{1/3} \iota_e^{1/2} \hat{d}_\beta$, $P_E = \tau_R/\tau_E$, and $P_\varphi = \tau_R/\tau_\varphi$. Here, τ_R is the resistive diffusion timescale, τ_H the hydrodynamic timescale, τ_E the energy confinement timescale, τ_φ the momentum confinement timescale, $S = \tau_R/\tau_H$ the Lundquist number, ω_E the $\mathbf{E} \times \mathbf{B}$ frequency, ω_{*e} the electron diamagnetic frequency, ω_{*i} the ion diamagnetic frequency, $\sqrt{\beta} = \sqrt{(5/3) \mu_0 p}/B_z$ the ratio of the sound speed to the Alfvén speed, p the plasma pressure, $d_\beta = c_\beta d_i$ the ion sound-radius, and d_i the collisionless ion skin-depth. Moreover, P_E and P_φ are magnetic Prandtl
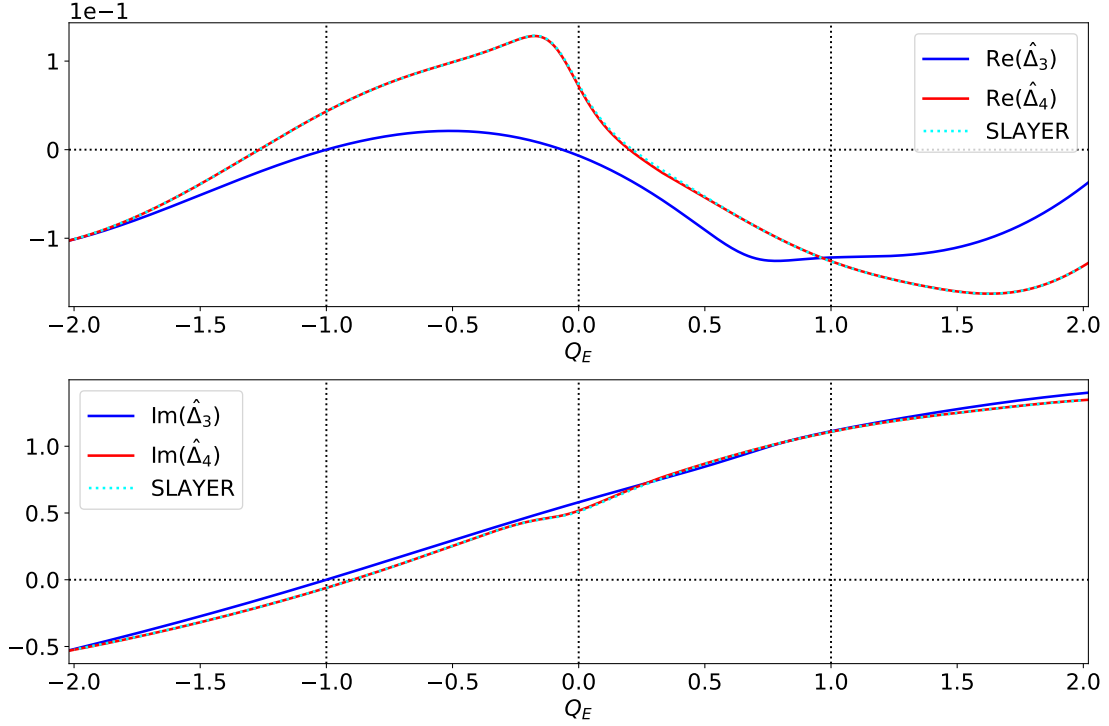
Figure 1: The scaled layer response index, $\hat{\Delta}$, plotted as a function of the normalized $\mathbf{E} \times \mathbf{B}$ frequency, Q_E, in the first Hall-resistive (HRi) response regime. See Table 1. $\hat{\Delta}_3$ is the response index predicted by the three-field Fourier-space response model of Ref. [17]. $\hat{\Delta}_4$ is the response index predicted by the four-field Fourier-space response model specified in Appendix A. SLAYER is the response index predicted by the four-field configuration-space response model of Ref. [18]. The three vertical lines indicate the electron fluid resonance, $Q_E + Q_e = 0$, the MHD fluid resonance, $Q_E = 0$, and the ion fluid resonance, $Q_E + Q_i = 0$, respectively, in order from the left to the right.

numbers, $\iota_e = -\omega_{*e}/(\omega_{*i} - \omega_{*e})$, and $\hat{d}_\beta = d_\beta/r_s$. All quantities are evaluated at the rational surface. (See Appendix A for more detailed definitions.)

Note that the previous definitions are slightly different to those adopted in Lee et alia [18]. We can convert our dimensionless parameters into into those used in Ref. [18] by letting $Q_E \to Q$, $Q_e \to -Q_{*e}$, $Q_i \to -Q_{*i}$, $\iota_e \to 1/(1+\tau)$, $P_E \to c_\beta^2$, and $P_\varphi \to P$.

3.3   Method of solution

After linearization and Fourier transformation (with respect to $x = r - r_s$), our four-field equations can be converted into the Ricatti matrix differential equation

$$p \, \frac{d\underline{\underline{W}}}{dp} = \underline{\underline{W}} - \underline{\underline{W}}\,\underline{\underline{W}} - \underline{\underline{E}}\,\underline{\underline{W}} + \underline{\underline{F}}. \tag{6}$$

Here, p is the Fourier transform variable, and $\underline{\underline{W}}(p)$ the 2×2 solution matrix. The elements of the 2×2 matrices $\underline{\underline{E}}(p)$ and $\underline{\underline{F}}(p)$ are specified in Eqs. (102)–(105) and (106)–(109), respectively. The method of solution is as follows. A solution of the Ricatti equation is launched from a large (with respect to unity) value of p, with the initial solution matrix specified in Eq. (166), and is then integrated to a small (with respect to unity) value of p. The *scaled layer response index*, $\hat{\Delta}$, is then deduced from the small-p elements of the solution matrix by means of Eq. (130). The true layer response index is $\Delta_s = S^{1/3} \, \hat{\Delta}$.
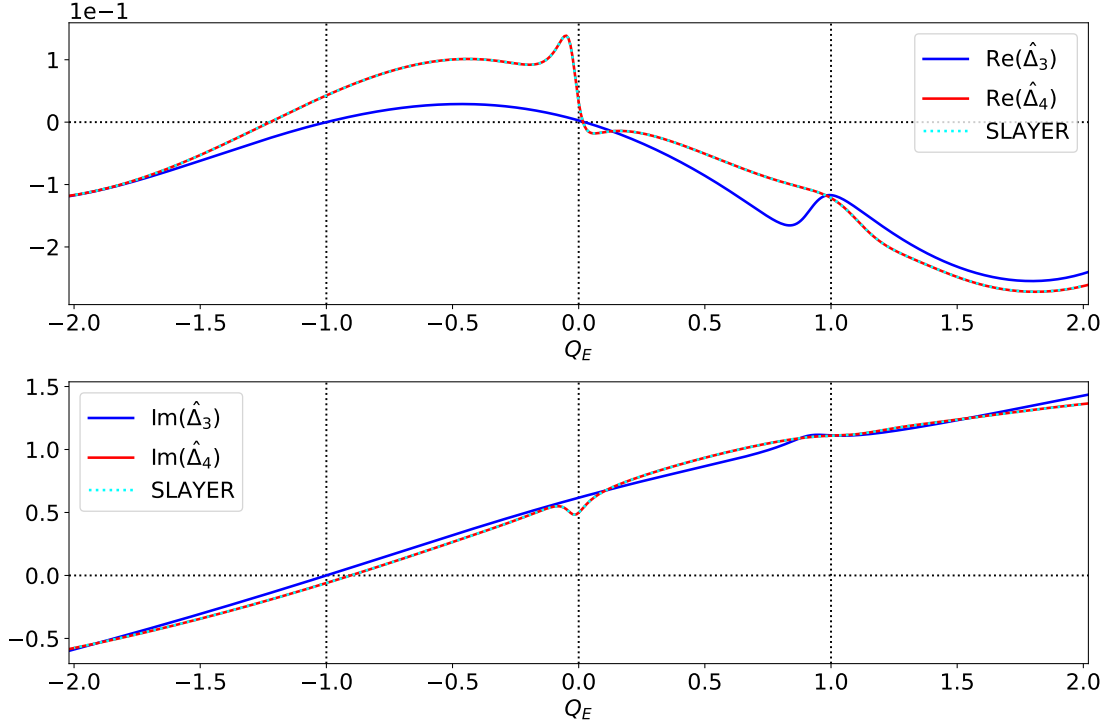
5

Figure 2: The scaled layer response index, $\hat{\Delta}$, plotted as a function of the normalized $\mathbf{E} \times \mathbf{B}$ frequency, Q_E, in the second Hall-resistive (HRii) response regime. See Table 1 and the caption to Fig. 1.

3.4 Benchmarking against SLAYER

Our first task is to benchmark the results of our Fourier-space calculation of $\hat{\Delta}$ against the results of the configuration-space calculation performed by Lee et alia. The latter calculation has been implemented in the SLAYER code [18, 20].

Figures 1–4 show the scaled layer response index, $\hat{\Delta}$, calculated as a function of the normalized $\mathbf{E} \times \mathbf{B}$ frequency, Q_E, by three different solution methods, in four of the analytic layer response regimes identified in Ref. [14]. These response regimes are the most probable ones for a comparatively weakly rotating tokamak plasma such as ITER. The dimensionless layer parameters used in the four response regimes are specified in Table 1. The first solution method involves using the Fourier-space analysis of Ref. [17]. In this analysis, the term involving c_β^2 is neglected in Eq. (57). Consequently, Eq. (59) decouples from Eqs. (56)–(58), which effectively converts a four-field response model (the four fields being $\bar{\psi}$, $\bar{N}$, $\bar{\phi}$, and $\bar{V}$) into a three-field response model (the three fields being $\bar{\psi}$, $\bar{N}$, and $\bar{\phi}$). The second solution method involves using the Fourier-space analysis set out in Appendix A. This method solves Eqs. (56)–(59), with no neglected terms, and thus constitutes a four-field response model. The first two methods have been implemented in the TJ code [28, 29]. The third solution method involves using the configuration-space analysis of Ref. [18], which is implemented in the SLAYER code [20]. Solution methods two and three constitute equivalent four-field response models.

It is clear from Figs. 1–4 that the second and third solution methods yield exactly the same results. This is remarkable because the second method involves solving four, coupled, first-order o.d.e.s in Fourier space, whereas the third involves solving ten, coupled, first-order o.d.e.s in configuration space. Moreover, as is clear from a comparison of Appendix A and Ref. [18], the analysis that leads to the four coupled equations in the former method is radically different from, and completely independent of, that which leads to the
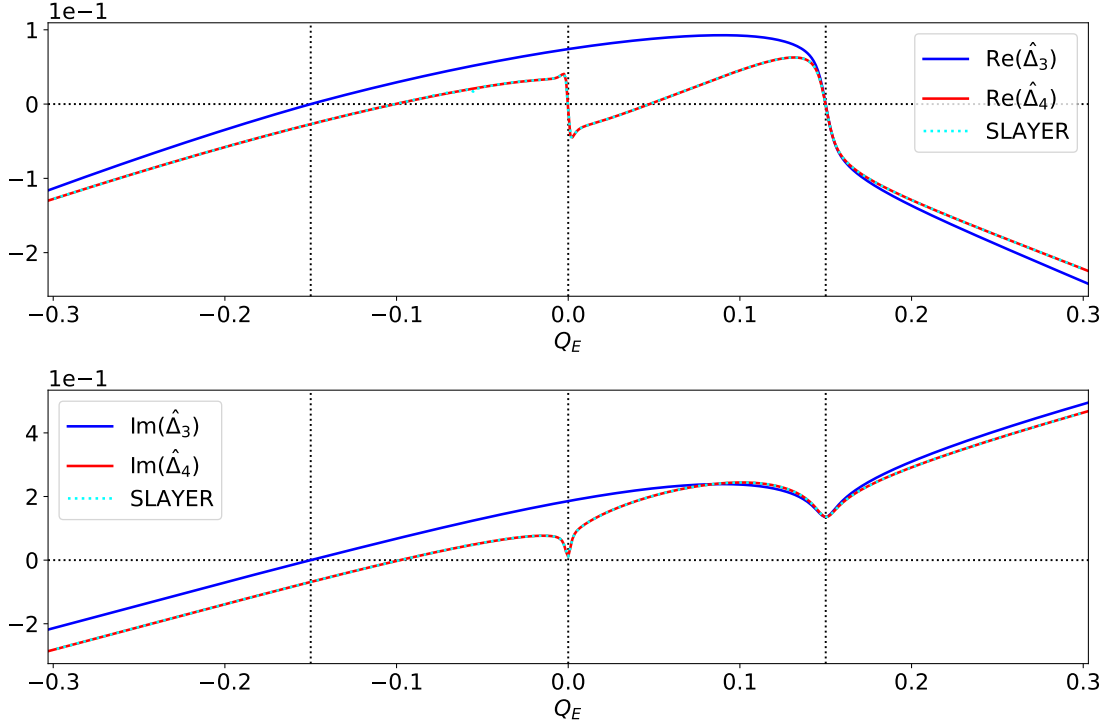
Figure 3: The scaled layer response index, $\hat{\Delta}$, plotted as a function of the normalized $\mathbf{E} \times \mathbf{B}$ frequency, Q_E, in the second resistive-inertial (RIii) response regime. See Table 1 and the caption to Fig. 1.

ten coupled equations in the latter method. It follows that the two solution methods constitute strong independent checks on one another. Hence, we can be confident that the two methods are valid, and also that they have been implemented correctly in the TJ and SLAYER codes.

3.5   Effect of c_β

In Figs. 1–4, the *electron fluid resonance*, $Q_E + Q_e = 0$, the *MHD-fluid resonance*, $Q_E = 0$, and the *ion fluid resonance*, $Q_E + Q_i = 0$, are indicated. The electron fluid resonance corresponds to the situation in which the rotation frequency of the electron fluid at the rational surface passes through zero, which we would expect to maximize the interaction between the electron fluid and the static RMP. Likewise for the other fluid resonances.

Figures 1–4 allow us to assess the consequences of neglecting the term involving c_β^2 in Eq. (57) by looking at the difference between the four-field and the three-field scaled layer response indices, $\hat{\Delta}_4$ and $\hat{\Delta}_3$, respectively. Obviously, this neglect is unlikely to make a significant difference if the ion sound parameter, c_β, is much less than unity, which explains why the rather large value, $c_\beta = 1$, is used in the calculations shown in the figures. (See Table 1.) It can be seen from the figures that the neglect of the c_β^2 term has a larger relative effect on the real part of the scaled layer response index, $\hat{\Delta}$, than on the imaginary part. Furthermore, Figs. 2 and 3 indicate that if the c_β^2 term is neglected then the plasma response model fails to capture resonant behavior that occurs, in some response regimes, close to the MHD-fluid resonance ($Q_E = 0$). All four figures indicate that if the c_β^2 term is neglected then the real and the imaginary parts of the scaled response index pass simultaneously through zero at the electron fluid resonance ($Q_E + Q_e = 0$). From Eq. (5), this implies a complete loss of shielding at the electron fluid resonance, leading to a vacuum-like response in which the reconnected magnetic flux driven at the rational surface is maximized. The figures also indicate
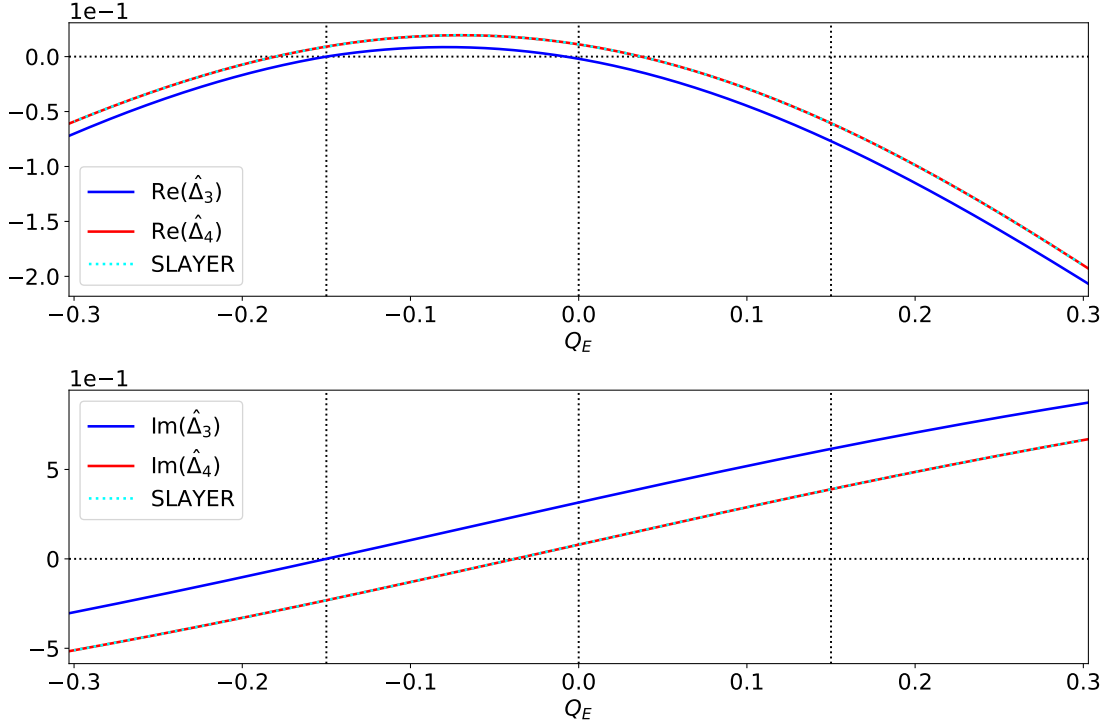
7

Figure 4: The scaled layer response index, $\hat{\Delta}$, plotted as a function of the normalized $\mathbf{E} \times \mathbf{B}$ frequency, Q_E, in the second viscous-resistive (VRii) response regime. See Table 1 and the caption to Fig. 1.

that if the c_β^2 term is retained then the value of Q_E at which the imaginary part of the scaled response index passes through zero shifts from the electron fluid resonance in the direction of the ion fluid resonance [18]. The value of Q_E at which the real part of the scaled response index passes through zero also shifts from the electron fluid resonance. However, the direction of the shift is different in different response regimes.

Figure 5 shows the difference between the scaled layer response index predicted by the four-field, Fourier-space, resonant response model of Appendix A and the three-field (i.e., $c_\beta = 0$), Fourier-space, resonant response model of Ref. [17], plotted as a function of the normalized $\mathbf{E} \times \mathbf{B}$ frequency, Q_E. The calculations are performed using the Q_e, Q_i, D, P_E, and P_φ values associated with the VRii regime of Table 1, and for various different values of c_β. It can be seen that the difference between the predictions of the four-field and three-field models is an increasing function of increasing c_β, and that the difference is essentially negligible for c_β values less than 0.01.

Figure 6 shows the critical values of the normalized electron fluid rotation frequency at the rational surface, $Q_E + Q_e$, at which the real and imaginary parts of the (four-field) scaled layer response index, $\hat{\Delta}$, pass through zero, plotted as functions of c_β. The calculations are performed using the Q_e, Q_i, D, P_E, and P_φ values associated with the HRi, HRii, RIii, and VRii regimes of Table 1. As we have seen, if $c_\beta = 0$ then the real and the imaginary parts of $\hat{\Delta}$ pass through zero simultaneously as the electron fluid rotation frequency passes through zero. However, the figure indicates that, as c_β increases from zero, the critical value of the electron fluid rotation frequency at which the real part of the scaled layer response index passes through zero shifts in the electron diamagnetic direction (i.e., to more negative values of $Q_E + Q_e$), whereas that at which the imaginary part passes through zero shifts in opposite direction. The only exception to this rule occurs in the second resistive-inertial (RIii) regime, where the critical values of the electron fluid rotation frequency at which the real and imaginary parts of the scaled layer response index pass through zero both shift in the ion diamagnetic direction by almost equal amounts. According to Eq. (5), a vacuum
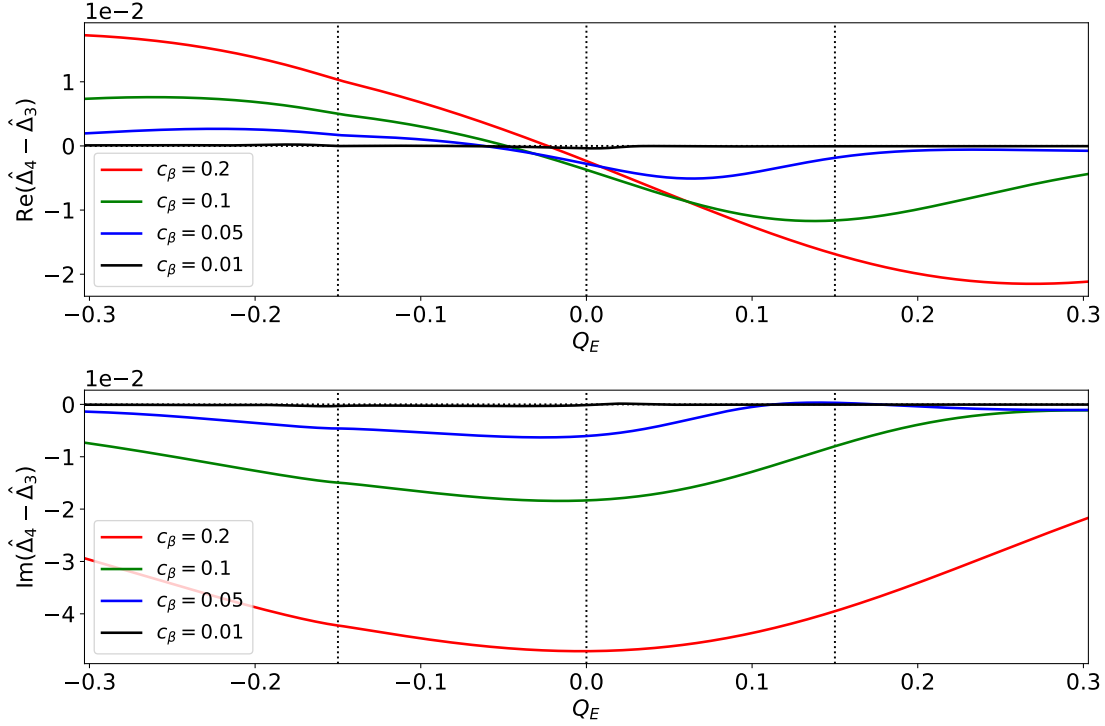
Figure 5: The difference between the scaled layer response indices predicted by the four-field and the three-field Fourier-space resonant response models, $\hat{\Delta}_4$ and $\hat{\Delta}_3$, respectively, plotted as a function of the normalized $\mathbf{E} \times \mathbf{B}$ frequency, Q_E. The calculations are performed in the VRii regime of Table 1, but for various different values of c_β. See the caption to Fig. 1.

response to the RMP (i.e., $\Psi \simeq \Psi_v$) requires the real and the imaginary parts of the scaled layer response index to be simultaneously much smaller than unity. This follows because the true layer response index is $\Delta_s = S^{1/3} \hat{\Delta}$. Furthermore,, under normal circumstances, $-E_{ss} \sim \mathcal{O}(1)$ and $S^{1/3} \gg 1$. As c_β increases, the state of affairs in which the real and imaginary parts of $\hat{\Delta}$ are simultaneously small (which, if $c_\beta = 0$, is automatically achieved when the electron fluid rotation frequency is zero) becomes progressively harder to achieve, as a consequence of the aforementioned frequency shifts, except in the RIii regime. The main difference between the RIii regime, and the other three response regimes, is the much smaller value of P_φ in the former regime. However, we expect $P_\varphi > 1$ in a conventional tokamak plasma (because the resistive diffusion timescale generally exceeds the momentum confinement timescale, unless the electron temperature much less than the on-axis temperature). Hence, we deduce that the frequency-shift behavior exhibited in Fig. 6 by the HRi, HRii, and VRii response regimes is more likely to represent the response of an actual tokamak plasma than that exhibited by the RIii regime.

4 Response of the pedestal region of tokamak plasma to an RMP

4.1 Edge-localized modes

Magnetically diverted tokamak plasmas (i.e., plasmas whose boundary is defined by a magnetic X-point) generally operate in so-called *H-mode* [30]. In this mode of operation, a transport barrier forms in the outer part of the plasma, leading to a region of enhanced density and temperature gradients known as the *pedestal*. As the name suggests, the "pedestal" is characterized by negative steps in the density and temperature
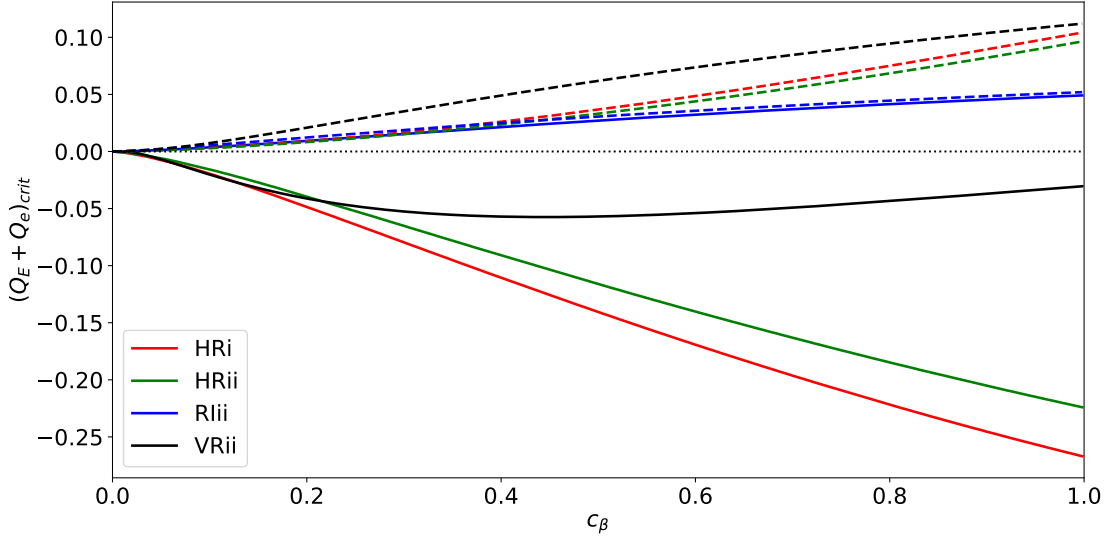
Figure 6: The critical value of the normalized electron fluid rotation frequency at the rational surface, $Q_E + Q_e$, at which the real (solid curves) and imaginary (imaginary curves) parts of the layer response index pass through zero, plotted as a function of c_β for the four response regimes specified in Table 1.

profiles that are located just inside the plasma boundary. (See Fig. 7.) Unfortunately, the large pressure gradient present in the pedestal can drive ideal-MHD instabilities known as *peeling-ballooning modes* [31]. Consequently, most H-mode plasmas exhibit intermittent bursts of heat and particle transport, emanating from the pedestal, that are known as (type-I) *edge-localized modes* (ELMs) [32]. It is estimated that the heat load that ELMs will deliver to the tungsten plasma-facing components in a reactor-scale tokamak will be large enough to cause massive tungsten ion influx into the plasma core, and that the erosion associated with this process will unacceptably limit the lifetimes of these components [33]. Consequently, the development of robust and effective methods for ELM control is a high priority for the international magnetic fusion program.

4.2   RMP-induced ELM suppression

The most promising method for the control of ELMs is via the application of externally generated, static RPMs to the plasma, Complete RMP-induced ELM suppression was first demonstrated on the DIII-D tokamak [7]. Subsequently, either mitigation or complete suppression of ELMs via RMPs has been demonstrated on the JET [34], ASDEX-U [35], KSTAR, [36] MAST [37], EAST [38], and MAST-U [39] tokamaks.

If an RMP opens up a magnetic island chain at the foot of the pedestal then it gives rise to an undesirable phenomenon, known as a *density pump-out*, by which the density gradient in the pedestal is greatly reduced [40, 41, 42]. On the other hand, if an RMP opens up a magnetic island chain at the top of the pedestal then it generally suppresses ELMs, while preserving the pedestal density and temperature gradients [40, 41, 42, 43, 44]. ELM suppression occurs because the island chain limits the width and height of the pedestal, and, thereby, prevents the peeling-ballooning instability threshold from being crossed [31].

In the following, we shall construct a simple model of a pedestal in the ITER tokamak, and then use our Fourier-space, four-field, resonant plasma response model to gauge the response of this pedestal to an externally generated, static RMP.

$$
\begin{array}{|ll|ll|ll|ll|ll|}
\nu_q & 3.5 & \nu_{n_e} & 1.1 & \nu_{T_e} & 2.0 & \nu_{T_i} & 2.0 & R_0 & 6.2\,\mathrm{m} \\
q_0 & 1.01 & n_{e\,0} & 1.2\times10^{20}\ \mathrm{m}^{-3} & T_{e\,0} & 1.6\times10^{4}\ \mathrm{eV} & T_{i\,0} & 1.4\times10^{4}\ \mathrm{eV} & a & 2.0\,\mathrm{m} \\
\alpha_q & 0.4 & n_{e\,1} & 2.0\times10^{19}\ \mathrm{m}^{-3} & T_{e\,1} & 0.0\times10^{0}\ \mathrm{eV} & T_{i\,1} & 2.5\times10^{1}\ \mathrm{eV} & B_z & 5.3\,\mathrm{T} \\
\Delta_q & 0.6 & \Delta_{n_e} & 9.0\times10^{19}\ \mathrm{m}^{-3} & \Delta_{T_e} & 4.0\times10^{3}\ \mathrm{eV} & \Delta_{T_i} & 4.0\times10^{3}\ \mathrm{eV} & \chi_E & 1.0\,\mathrm{m}^2/\mathrm{s} \\
\hat{r}_q & 0.940 & \hat{r}_{n_e} & 0.950 & \hat{r}_{T_e} & 0.955 & \hat{r}_{T_i} & 0.950 & \chi_\varphi & 1.5\,\mathrm{m}^2/\mathrm{s} \\
\delta_q & 0.025 & \delta_{n_e} & 0.025 & \delta_{T_e} & 0.025 & \delta_{T_i} & 0.025 & Z_{\mathrm{eff}} & 3.0 \\
\end{array}
$$

Table 2: Parameters used to model an ITER pedestal.

4.3 Model ITER pedestal

We shall again employ the cylindrical analysis of Sect. 2. Let the normalized toroidal plasma current take the form

$$
J_z(\hat{r}) = \frac{2}{q_0}\,(1-\hat{r}^{\,2})^{\nu_q-1}, \tag{7}
$$

where $\hat{r}=r/a$. The model safety-factor profile is written

$$
q(\hat{r}) = \frac{\nu_q\,q_0\,\hat{r}^{\,2}}{1-(1-\hat{r}^{\,2})^{\nu_q}} - \alpha_q\,\ln(1-\hat{r}^{\,2}) - \frac{\Delta_q}{2}\left[1+\tanh\left(\frac{\hat{r}-\hat{r}_q}{\delta_q}\right)\right]. \tag{8}
$$

The first term on the right-hand side of the previous equation is the safety-factor profile that conventional cylindrical theory would associate with the current profile specified in Eq. (7) [27]. Here, q_0 is the cylindrical safety-factor on the magnetic axis ($\hat{r}=0$), whereas $\nu_q\,q_0$ is the cylindrical safety-factor at the plasma boundary ($\hat{r}=1$). The second term mimics the logarithmic singularity in the safety-factor profile that occurs at the edge of a magnetically diverted plasma (assuming that the magnetic separatrix corresponds to $\hat{r}=1$) [25]. The final term represents the reduction in the magnetic shear generated by the strongly peaked, pressure-gradient-driven, bootstrap current [45] present in the pedestal of an H-mode plasma. (See, for example, Fig. 6 of Ref. [46], Fig. 1 of Ref. [47], and Fig. 2 of Ref. [48].) The approach taken here is similar to that taken in the TM1 code, which employs cylindrical geometry in association with experimental safety-factor, density, and temperature profiles [49, 50]. The TM1 approach has been very successful at explaining RMP-induced density pump-out and ELM suppression in the DIII-D tokamak [40, 41, 42].

The model electron number density, electron temperature, and ion temperature profiles take the respective forms

$$
n_e(\hat{r}) = (n_{e\,0}-n_{e\,1})\,(1-\hat{r}^{\,2})^{\nu_{n_e}} + \frac{\Delta_{n_e}}{2}\left[1+\tanh\left(\frac{\hat{r}-\hat{r}_{n_e}}{\delta_{n_e}}\right)\right] + n_{e\,1}, \tag{9}
$$

$$
T_e(\hat{r}) = (T_{e\,0}-T_{e\,1})\,(1-\hat{r}^{\,2})^{\nu_{T_e}} + \frac{\Delta_{T_e}}{2}\left[1+\tanh\left(\frac{\hat{r}-\hat{r}_{T_e}}{\delta_{T_e}}\right)\right] + T_{e\,1}, \tag{10}
$$

$$
T_i(\hat{r}) = (T_{i\,0}-T_{i\,1})\,(1-\hat{r}^{\,2})^{\nu_{T_i}} + \frac{\Delta_{T_i}}{2}\left[1+\tanh\left(\frac{\hat{r}-\hat{r}_{T_i}}{\delta_{T_i}}\right)\right] + T_{i\,1}. \tag{11}
$$

Here, the second terms on the right-hand sides of the previous three equations represent the negative steps in the three profiles in the pedestal region.

The parameters used in our model ITER pedestal are specified in Table 2. The model profiles are shown in Fig. 7. The electron number density and electron and ion temperature profiles approximately reproduce the profiles shown in Fig. 8 of Ref. [51]. Our model pedestal is characterized by $q_{95}=3.70$, $n_e(1)=2.2\times10^{19}\ \mathrm{m}^{-3}$, $T_e(1)=106\,\mathrm{eV}$, and $T_i(1)=97\,\mathrm{eV}$. The magnetic shear attains its minimum value of $s=0.21$ at $\hat{r}=0.937$.

The parallel electrical resistivity of the plasma is [21]

$$
\eta_\|(\hat{r}) = \frac{0.51\,\ln\Lambda\,Z_{\mathrm{eff}}\,m_e^{1/2}\,e^{1/2}}{6\sqrt{2}\,\pi^{3/2}\,f_p\,\epsilon_0^2\,T_e^{3/2}} \tag{12}
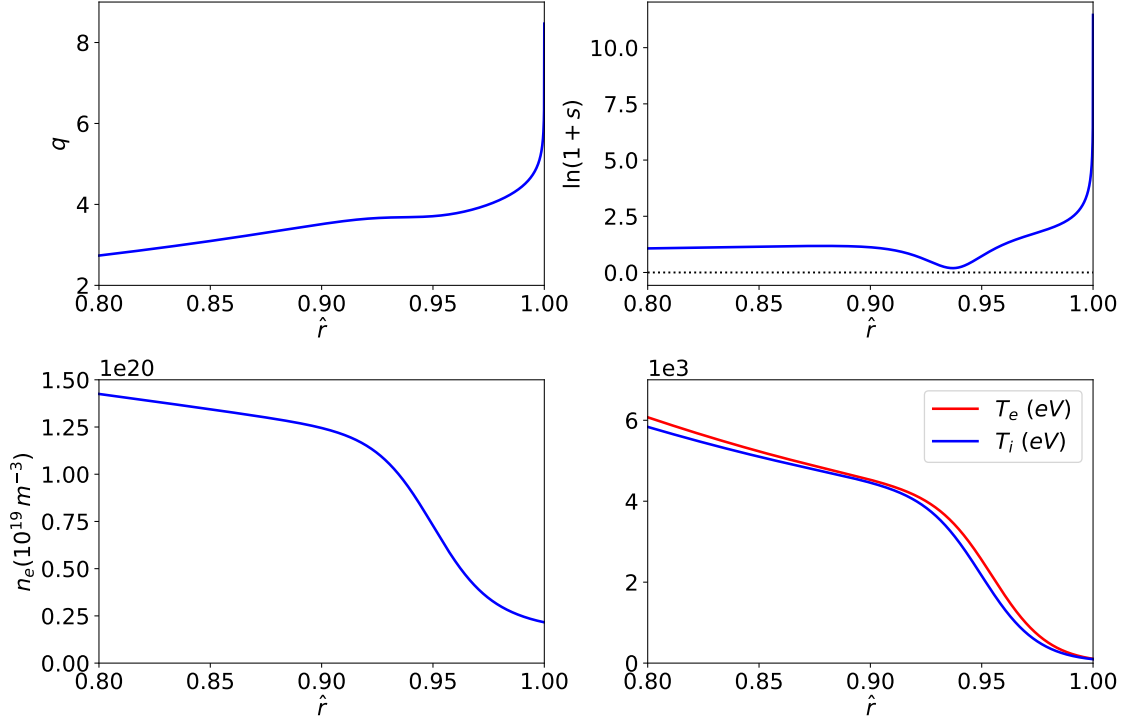$$

11

Figure 7: Equilibrium safety-factor, q, magnetic shear, s, electron number density, n_e, electron temperature, T_e, and ion temperature, T_i, profiles used to model an ITER pedestal.

where

$$\ln \Lambda(\hat{r}) = 24 - \ln \left[\left(\frac{n_e}{10^6} \right)^{1/2} \frac{1}{T_e} \right], \tag{13}$$

$$f_p(\hat{r}) = 1 - 1.46 \left(\frac{\hat{r}\,a}{R_0} \right)^{1/2} + 0.46 \left(\frac{\hat{r}\,a}{R_0} \right)^{3/2}. \tag{14}$$

Here, n_e is measured in SI units, whereas T_e is measured in units of eV. Moreover, m_e is the electron mass, e the magnitude of the electron charge, $Z_{\text{eff}} = 3.0$ the effective ion charge number, $R_0 = 6.2\,\text{m}$ the plasma major radius, and $a = 2.0\,\text{m}$ the plasma minor radius [52]. The factor f_p accounts for the neoclassical enhancement of resistivity [53].

All of the remaining plasma parameters, apart from the $\mathbf{E} \times \mathbf{B}$ rotation profile, can be calculated from their definitions given in Appendix A, the profile data specified in Eqs. (8)–(14) and Table 2, and the following information. The toroidal magnetic field-strength is $B_z = 5.3\,\text{T}$ [52], the ion mass number is $M = 2$, and the perpendicular energy and momentum diffusivities take the (spatially) constant values $\chi_E = 1.0\,\text{m}^2/\text{s}$ and $\chi_\varphi = 1.5\,\text{m}^2/\text{s}$, respectively [54].

Figure 8 shows the rotation frequency profiles in our model ITER pedestal. The adopted $\mathbf{E} \times \mathbf{B}$ frequency profile is written

$$\omega_E(\hat{r}) = \omega_{E\,0} \left(1 - \hat{r}^{\,2} \right)^{\nu_E} + \alpha_E \, \omega_{*\,e}(\hat{r}), \tag{15}$$

where $\omega_{E\,0} = 3 \times 10^4\,\text{rad./s}$, $\nu_E = 1.1$, and $\alpha_E = 0.3$. This frequency profile has the appropriate sign in the pedestal and the core [47, 51], and is designed to ensure that the electron fluid rotation frequency, $\omega_{\perp e} \equiv \omega_E + \omega_{*e}$, passes through zero close to the top of the pedestal. This feature of the electron fluid rotation frequency is almost always observed in H-mode tokamak plasmas with co-current neutral beam injection, and has been identified as a key feature in RMP-induced ELM suppression [40, 41, 42, 43, 44].
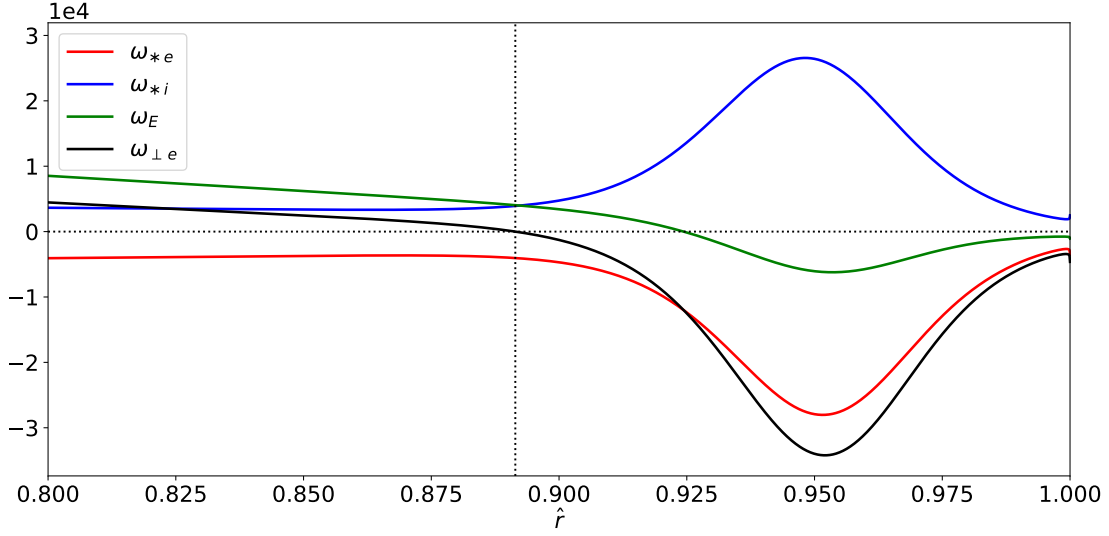
Figure 8: Rotation frequency profiles in a model ITER pedestal. Here, ω_{*e} is the electron diamagnetic frequency, ω_{*i} the ion diamagnetic frequency, ω_E the $\mathbf{E} \times \mathbf{B}$ frequency, and $\omega_{\perp e} \equiv \omega_E + \omega_{*e}$ the electron fluid rotation frequency. The vertical dotted line indicates the radius at which $\omega_{\perp e} = 0$. All frequencies are measured in units of radians per second.

4.4 q_{95} scan

The *normalized poloidal magnetic flux* is conventionally defined as $\Psi_N(\hat{r}) = \psi_p(\hat{r})/\psi_p(1)$, where the poloidal magnetic flux, $\psi_p(\hat{r}) = B_z\, a^2 \int_0^{\hat{r}} d\hat{r}'\hat{r}'/q(\hat{r}')$, is calculated from Eq. (8). Thus, $\Psi_N = 0$ at the magnetic axis, and $\Psi_N = 1$ at the magnetic separatrix (i.e., the magnetic flux-surface that contains the magnetic X-point). Magnetically diverted plasmas are conventionally characterized by q_{95}, which is defined as the safety-factor value at the magnetic flux-surface that contains 95% of the poloidal magnetic flux contained by the magnetic separatrix. In other words, $q_{95} = q(\hat{r}_{95})$, where $\Psi_N(\hat{r}_{95}) = 0.95$. We can vary q_{95}, at constant on-axis safety-factor, q_0, by varying the parameter ν_q, appearing in Eq. (8), while keeping all other parameters in our model fixed.

Suppose that the RMP can be decomposed into of a set of helical Fourier harmonics with a common toroidal mode number, $n = 1$, but a range of different poloidal mode numbers, m. In our study, we shall concentrate on $n = 1$ rational surfaces associated with intrinsically stable tearing modes whose poloidal mode numbers lie in the range $4 \leq m \leq 11$, and which are located in the region $0 < \Psi_N < 0.9999$. The parameter ν_q is varied from 2.01 to 16.4, which causes q_{95} to vary from about 2.4 to 14.5. Figure 9 shows the normalized minor radii, $\hat{r}$, of the various $n = 1$ rational surfaces, plotted as functions of q_{95}. It can be seen that, as q_{95} increases, successive rational surfaces emerge from the magnetic separatrix, and sweep across the pedestal region.

Figure 9 also shows the tearing stability indices, E_{ss}, associated with the $n = 1$ rational surfaces, plotted as functions of the rational surface radii. It can be seen that the indices are all negative (confirming that the plasma is intrinsically tearing stable). Note that E_{ss} is calculated from the cylindrical tearing mode equation, (1), using the normalized current profile (7) and the safety-factor profile (8).

Figure 10 shows the real and imaginary parts of the layer response indices, Δ_s, associated with the $n = 1$ rational surfaces, plotted as functions of the rational surface radii, $\hat{r}$. Now, it is clear from the analysis of Ref. [25] that $|\Delta_s| \propto |s|^{-1/2}$. According to Fig. 7, as $\hat{r}$ decreases from unity (i.e., as we move from the magnetic separatrix into the interior of the plasma), the magnetic shear, s, decreases from a very large initial value, attains a minimum value in the center of the pedestal ($\hat{r} \simeq 0.95$), and then increases to
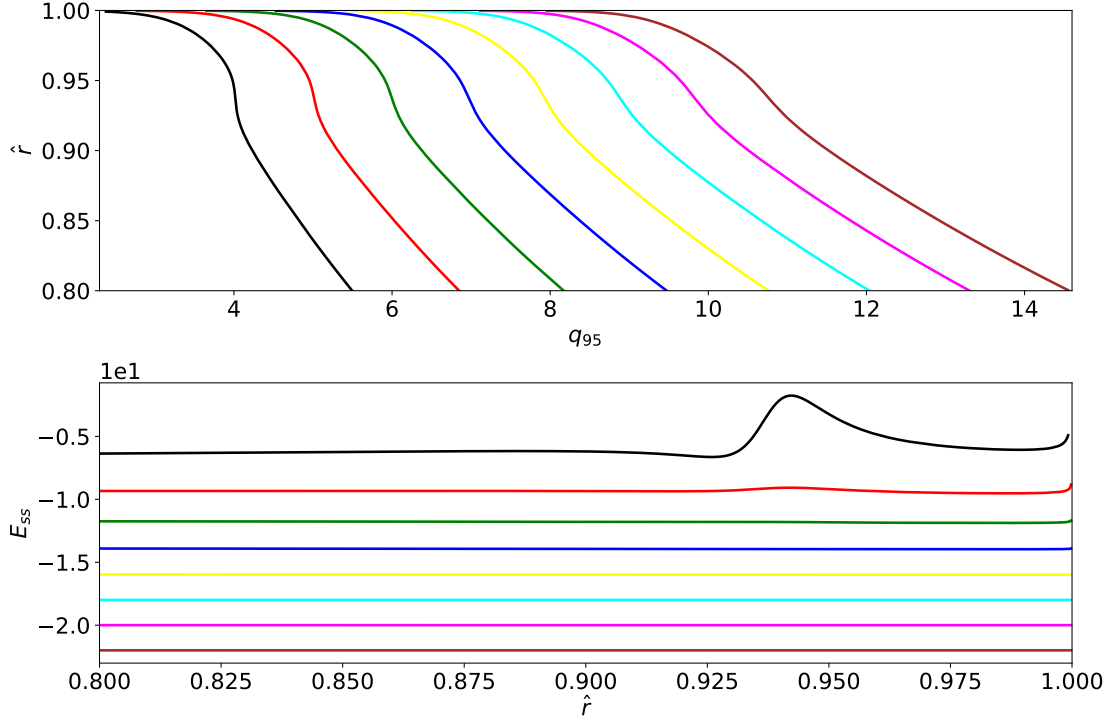
13

Figure 9: Top panel: Normalized minor radii, $\hat{r}$, of the $n = 1$ rational surfaces plotted as functions of q_{95} in a model ITER pedestal. Bottom panel: Stability indices, E_{ss}, of tearing modes resonant at the $n = 1$ rational surfaces, plotted as functions of the normalized minor radii, $\hat{r}$, of the surfaces, in a model ITER pedestal. Different colored curves correspond to different poloidal mode numbers according to the legend in Fig. 12.

reach a comparatively modest approximately constant value. The very large magnetic shear just inside the separatrix is due to the presence of the magnetic X-point on the separatrix [25]. The minimum in the shear is caused by the strongly peaked bootstrap current at the center of the pedestal (i.e., where the density and temperature gradient attain their peak values). It is apparent from Fig. 10 that, as the rational surface radius, $\hat{r}$, decreases from unity, the inverse dependence of the layer response index on the magnetic shear causes the magnitude of the index to rise strongly from a very small initial value, to then decrease and attain a minimum value at the center of the pedestal, and to then increase to reach a very large value [i.e., $|\Delta_s| \sim \mathcal{O}(10^3)$].

It is helpful to define the *shielding factor* at a given rational surface:

$$\Sigma = \left| 1 + \frac{\Delta_s}{(-E_{ss})} \right| - 1. \tag{16}$$

It follows from the layer response equation, (5), that

$$\frac{|\Psi_s|}{|\Psi_v|} = \frac{1}{1 + \Sigma}. \tag{17}$$

Thus, if $\Sigma \ll 1$ then we obtain a vacuum response characterized by $|\Psi_s| \simeq |\Psi_v|$ (i.e., characterized by no suppression of driven magnetic reconnection). On the other hand, if $\Sigma \gg 1$ then we obtain an ideal response characterized by $|\Psi_s| \ll |\Psi_v|$ (i.e., characterized by strong suppression of driven magnetic reconnection). Figure 11 shows the shielding factors, Σ, associated with the $n = 1$ rational surfaces, plotted as functions of the rational surface radii, $\hat{r}$. It can be seen that, as $\hat{r}$ decreases from unity, the shielding factor rises strongly
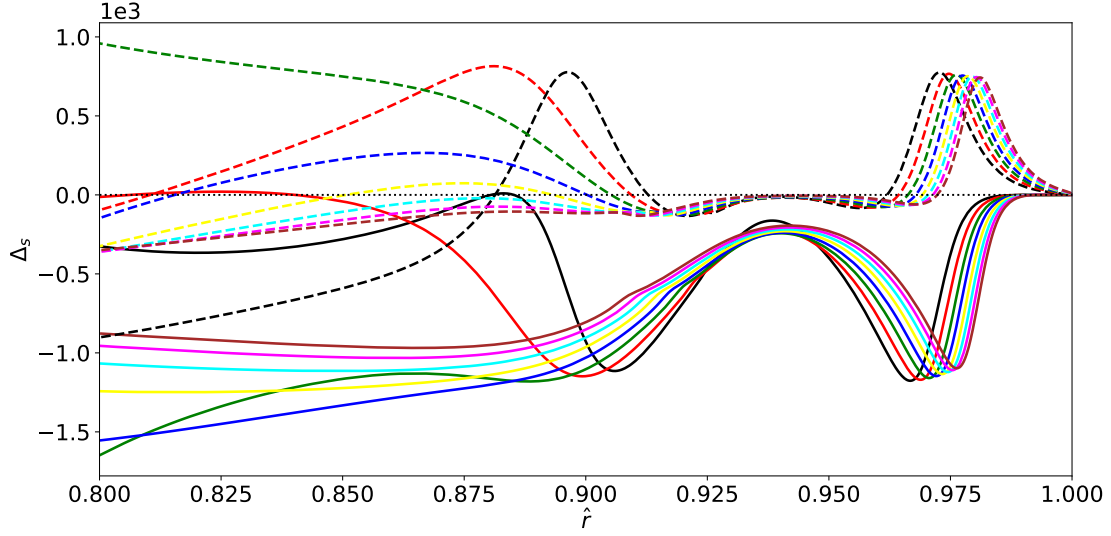
14

Figure 10: The real (solid curves) and imaginary (dashed curves) parts of the layer response indices, Δ_s, at the $n = 1$ rational surfaces, plotted as functions of the normalized minor radii, $\hat{r}$, of the surfaces, in a model ITER pedestal. Different colored curves correspond to different poloidal mode numbers according to the legend in Fig. 12.

from a very small initial value, then decreases and attains a minimum value at the center of the pedestal, and then increases to reach a large value [i.e., $\Sigma \sim \mathcal{O}(10^2)$]. The very small value of the shielding factor just inside the magnetic separatrix is ultimately caused by the very large magnetic shear in this region. Likewise, the minimum in the shielding factor at the center of the pedestal is caused by the minimum in the magnetic shear in this region.

According to the three-field ($c_\beta = 0$) layer response model of Ref. [17], the real and the imaginary parts of the layer response index simultaneously pass through zero at the magnetic flux-surface where the electron fluid rotation frequency, $\omega_{\perp e} \equiv \omega_E + \omega_{*e}$, reverses sign. The location of this flow-reversal surface, which lies close to the top of the pedestal, is indicated by the vertical dotted line in Fig. 11. Thus, according to Eq. (16), the three-field model predicts that the shielding factor, Σ, associated with every rational surface attains a minimum value of zero as the surface passes through the flow-reversal surface. In other words, the three-field model predicts a complete breakdown in the shielding of driven magnetic reconnection at every rational surface, as it passes through the flow-reversal surface. However, as is clear from Fig. 11, when the finite value of the ion sound parameter, c_β, is taken into account in the layer calculation (i.e., when we adopt a four-field layer response model), this picture changes substantially. In fact, only the rational surfaces associated with the $m = 4$ and $m = 5$ poloidal harmonics exhibit a breakdown in shielding close to the top of the pedestal. As is clear from Fig. 10, this breakdown occurs because the real and imaginary parts of the corresponding layer response indices pass through zero simultaneously. Note, in particular, from Figs. 10 and 11, that if the imaginary part of the layer response index passes through zero, but the real part does not, then there is no breakdown in shielding. Figure 11 also indicates that, as a consequence of finite c_β, the breakdown of shielding associated with the $m = 4$ and $m = 5$ rational surfaces occurs when the surfaces are shifted inward from the flow-reversal surface.

Figure 12 shows the shielding factors, Σ, associated with the $n = 1$ rational surfaces at the very edge of the pedestal, plotted as functions of the normalized poloidal magnetic fluxes, Ψ_N, at the surfaces. It can be seen that, as a consequence of the very rapid increases in the magnetic shear, the shielding factors asymptote to zero as the magnetic separatrix is approached (i.e., as $\Psi_N \to 1$). In Ref. [25], it is argued that if $\Sigma < 1$ then the response of a rational surface to the RMP is essentially indistinguishable from that of
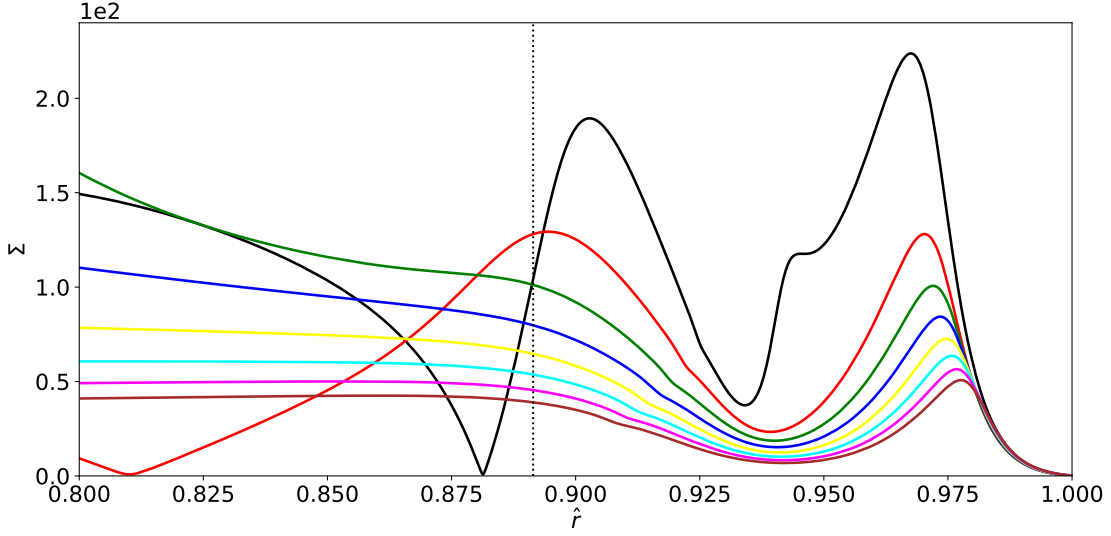
Figure 11: The shielding factors, Σ, at the $n = 1$ rational surfaces, plotted as functions of the normalized minor radii, $\hat{r}$, of the surfaces, in a model ITER pedestal. Different colored curves correspond to different poloidal mode numbers according to the legend in Fig. 12. The vertical dotted line indicates the radius at which $\omega_{\perp e} \equiv \omega_E + \omega_{*e} = 0$.

a vacuum, which allows us to neglect the responses of rational surfaces that are situated in a radially thin region, lying just inside the magnetic separatrix, that extends from $1 - \epsilon_c < \Psi_N < 1$. It is clear from the figure that $\epsilon_c \simeq 2 \times 10^{-3}$, which is similar to the value estimated in the three-field analysis of Ref. [25]. The fact that we can ignore rational surfaces that lie in the region $1 - \epsilon_c < \Psi_N < 1$ implies that we do not have to include an infinite number of surfaces in the calculation of the response of a magnetically diverted tokamak plasma to an RMP, despite the fact that the safety-factor asymptotes to infinity as the magnetic separatrix is approached.

The net toroidal electromagnetic torque exerted in the vicinity of a given rational surface takes the form [4]

$$T_\varphi = \frac{2\pi^2 R_0 n}{\mu_0} |\Psi_v|^2 \hat{T}_\varphi, \tag{18}$$

where

$$\hat{T}_\varphi = \frac{\text{Im}(\Delta_s)}{(1 + \Sigma)^2}. \tag{19}$$

Figure 13 shows the normalized toroidal electromagnetic torques, $\hat{T}_\varphi$, at the $n = 1$ rational surfaces, plotted as functions of the normalized minor radii, $\hat{r}$, of the surfaces. It can be seen that the torques are comparatively large very close to the magnetic separatrix because of the breakdown of the shielding of driven magnetic reconnection in this region. These large torques act to change the $\mathbf{E} \times \mathbf{B}$ rotation profile at the very edge of the plasma in such a manner as to further reduce the shielding in this region [4]. The breakdown of shielding at the very edge of the plasma is associated with the density pump-out phenomenon [40, 41, 42]. Figure 13 also indicates that the torques at the $m = 4$ and $m = 5$ rational surfaces become comparatively large when the shielding of driven magnetic reconnection at these surfaces breaks down close to the top of the pedestal. These large torques act to change the $\mathbf{E} \times \mathbf{B}$ rotation profile in such a manner as to further reduce the shielding [4]. The breakdown of shielding close to the top of the pedestal is associated with RMP-induced ELM suppression [40, 41, 42, 43, 44].
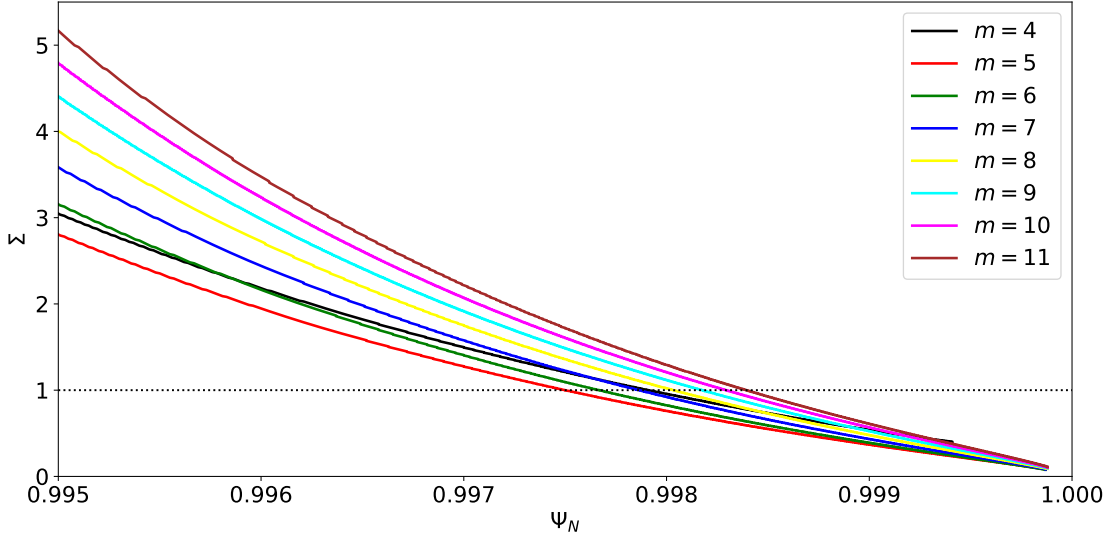
16

Figure 12: The shielding factors, Σ, at the $n = 1$ rational surfaces, plotted as functions of the normalized poloidal magnetic fluxes, Ψ_N, at the surfaces, in the outer part of a model ITER pedestal.

5 Summary

In this paper, we demonstrate that the two-fluid drift-MHD response of a resonant layer in a tokamak plasma to an externally generated, static RMP can be reduced to four, coupled, first-order o.d.e.s in Fourier space. We also show that these four equations can be conveniently solved by means of a Riccati transformation. (See Appendix A.) The Fourier-space, four-field, resonant plasma response model is successfully benchmarked against the equivalent configuration-space model of Lee et alia [18]. (See Sect. 3.) The Fourier-space model is used to estimate the response of an ITER pedestal to an RMP. (See Sect. 4.) We find that the strong magnetic shear present just inside the magnetic separatrix suppresses the response of the plasma to the RMP to such an extent that it is indistinguishable from that of a vacuum. Consequently, we can neglect rational surfaces that lie in the strong-shear region when calculating the response of the plasma to the RMP. This implies that it is not necessary to include an infinite number of rational surfaces in the calculation, despite the fact that the safety-factor asymptotes to infinity as the magnetic separatrix is approached. Furthermore, the vacuum response of the plasma in the strong-shear region is associated with the density pump-out phenomenon. The shielding of driven magnetic reconnection is also found to break down at rational surfaces associated with comparatively low poloidal mode numbers that are situated close to the top of the pedestal. This breakdown is associated with RMP-induced ELM suppression.
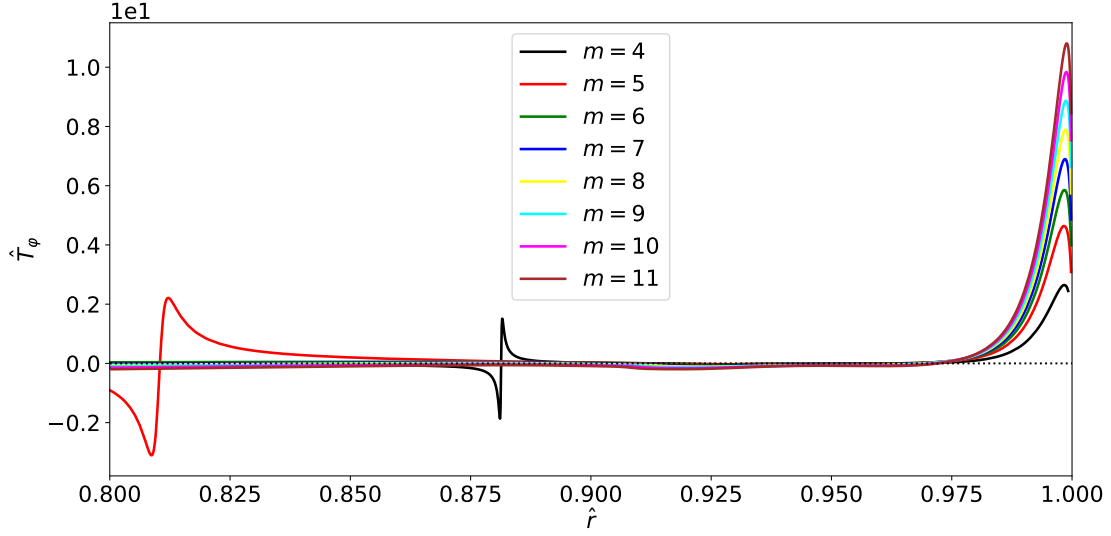
Acknowledgements

Funding

Figure 13: The normalized toroidal electromagnetic torques, $\hat{T}_\varphi$, at the $n = 1$ rational surfaces, plotted as functions of the normalized minor radii, $\hat{r}$, of the surfaces, in a model ITER pedestal.

Data availability statement

The data that support the findings of this study are available from the corresponding author upon reasonable request.

A Fourier-space four-field resonant plasma response model

A.1 Fundamental definitions

Consider the quasi-cylindrical plasma equilibrium introduced in Sect. 2.1. The plasma is assumed to consist of two species. First, electrons of mass m_e, electrical charge $-e$, number density n_e, and temperature T_e. Second, ions of mass m_i, electrical charge $+e$, number density n_e, and temperature T_i. Let $p = n_e (T_e + T_i)$ be the total plasma pressure.

Let r_s be the minor radius of the rational surface. It is helpful to define $n_0 = n_e(r_s)$, $p_0 = p(r_s)$, [21]

$$\eta_e = \left. \frac{d \ln T_e}{d \ln n_e} \right|_{r=r_s}, \tag{20}$$

$$\eta_i = \left. \frac{d \ln T_i}{d \ln n_e} \right|_{r=r_s}, \tag{21}$$

$$\iota \equiv \left(\frac{dp_e}{dp_i} \right)_{r_s} = \left(\frac{T_e}{T_i} \right)_{r=r_s} \left(\frac{1 + \eta_e}{1 + \eta_i} \right), \tag{22}$$

where $n_e(r)$, $p(r)$, $p_e(r)$, $p_i(r)$, $T_e(r)$, and $T_i(r)$ refer to electron number density, total pressure, electron pressure, ion pressure, electron temperature, and ion temperature profiles, respectively, in the absence of the magnetic perturbation.

For the sake of simplicity, the perturbed electron and ion temperature profiles are assumed to be functions of the perturbed electron number density profile in the immediate vicinity of the rational surface. In other words, $T_e = T_e(n_e)$ and $T_i = T_i(n_e)$. This implies that $p = p(n_e)$. The "MHD velocity", which is the velocity

18

of a fictional MHD fluid [55], is defined $\mathbf{V} = \mathbf{V}_E + V_{\parallel\,i}\,\mathbf{b}$, where $\mathbf{V}_E$ is the $\mathbf{E} \times \mathbf{B}$ drift velocity, $V_{\parallel\,i}$ the parallel component of the ion fluid velocity, $\mathbf{b} = \mathbf{B}/|\mathbf{B}|$, and $\mathbf{B}$ the magnetic field-strength.

A.2 Fundamental fields

The four fundamental fields in our four-field model—namely, ψ, N, ϕ, and V—have the following definitions [21]:

$$\nabla\psi = \frac{\mathbf{e}_{\parallel} \times \mathbf{B}}{r_s\,B_z}, \tag{23}$$

$$N = -\hat{d}_i\left(\frac{p - p_0}{B_z^2/\mu_0}\right), \tag{24}$$

$$\nabla\phi = \frac{\mathbf{e}_{\parallel} \times \mathbf{V}}{r_s\,V_A}, \tag{25}$$

$$V = \hat{d}_i\left(\frac{\mathbf{e}_{\parallel} \cdot \mathbf{V}}{V_A}\right). \tag{26}$$

Here, $\mathbf{e}_{\parallel} = (0,\, \epsilon/q_s,\, 1)$, $\epsilon = r/R_0$, $q_s = m/n$, $V_A = (B_z/\sqrt{\mu_0\,n_0\,m_i})_{r_s}$, $d_i = \sqrt{m_i/(n_0\,e^2\,\mu_0)}_{r_s}$, and $\hat{d}_i = d_i/r_s$. Our model also employs the auxiliary field

$$J = -\frac{2\,\epsilon_s}{q_s} + \hat{\nabla}^2\psi, \tag{27}$$

where $\epsilon_s = r_s/R_0$, and $\hat{\nabla} = r_s\,\nabla$. Note that V_A is the *Alfvén speed* at the rational surface, whereas d_i is the *collisionless ion skin-depth*.

A.3 Fundamental equations

For the case of a static (in the laboratory frame) magnetic perturbation, the four-field model takes the form [14, 15, 17, 21]:

$$0 = [\phi, \psi] - \iota_e\,[N, \psi] + \hat{\eta}_{\parallel}\,J + \hat{E}_{\parallel}, \tag{28}$$

$$0 = [\phi, N] + \hat{d}_{\beta}^2\,[J, \psi] + c_{\beta}^2\,[V, \psi] + \hat{\chi}_E\,\hat{\nabla}^2 N, \tag{29}$$

$$0 = [\phi, \hat{\nabla}^2\phi] - \frac{\iota_i}{2}\left(\hat{\nabla}^2[\phi, N] + [\hat{\nabla}^2\phi, N] + [\hat{\nabla}^2 N, \phi]\right) + [J, \psi] + \hat{\chi}_{\varphi}\,\hat{\nabla}^4(\phi + \iota_i\,N), \tag{30}$$

$$0 = [\phi, V] + [N, \psi] + \hat{\chi}_{\varphi}\,\hat{\nabla}^2 V. \tag{31}$$

Here, $[A, B] \equiv \hat{\nabla}A \times \hat{\nabla}B \cdot \mathbf{e}_{\parallel}$, $\iota_e = \iota/(1 + \iota)$, $\iota_i = 1/(1 + \iota)$, $\hat{t} = t/(r_s/V_A)$, $\hat{\eta}_{\parallel} = \eta_{\parallel}/(\mu_0\,r_s\,V_A)$, $\hat{E}_{\parallel} = E_{\parallel}/(B_z\,V_A)$, $\hat{\chi}_E = \chi_E/(r_s\,V_A)$, $\hat{\chi}_{\varphi} = \chi_{\varphi}/(r_s\,V_A)$, where $\eta_{\parallel}$ is the parallel plasma electrical resistivity at the rational surface, $E_{\parallel}$ the parallel inductive electric field that maintains the equilibrium toroidal plasma current in the vicinity of the rational surface, χ_E the anomalous perpendicular heat diffusivity at the rational surface, and χ_{φ} the anomalous perpendicular ion momentum diffusivity at the rational surface. Moreover, $d_{\beta} = c_{\beta}\,d_i$, and $\hat{d}_{\beta} = d_{\beta}/r_s$, where $c_{\beta} = [\beta/(1 + \beta)]_{r_s}^{1/2}$, and $\beta = (5/3)\,\mu_0\,p_0/B_z^2$. Here, d_{β} is usually referred to as the *ion sound-radius*.

A.4 Matching to plasma equilibrium

The unperturbed plasma equilibrium is such that $\mathbf{B} = (0,\, B_{\theta}(r),\, B_z)$, $p = p(r)$, $\mathbf{V} = (0,\, V_E(r),\, V_z(r))$, where $V_E(r) \simeq -E_r/B_z$ is the (dominant θ-component of the) $\mathbf{E} \times \mathbf{B}$ velocity. Now, the resonant layer is assumed to have a radial thickness that is much smaller than r_s. Hence, we only need to evaluate plasma

19

equilibrium quantities in the immediate vicinity of the rational surface. Equations (23)–(26) suggest that [21]

$$\psi(\hat{x}) = \frac{\hat{x}^2}{2\,\hat{L}_s}, \tag{32}$$

$$N(\hat{x}) = -\hat{V}_* \,\hat{x}, \tag{33}$$

$$\phi(\hat{x}) = -\hat{V}_E \,\hat{x}, \tag{34}$$

$$V(\hat{x}) = \hat{V}_\parallel, \tag{35}$$

where $\hat{x} = (r - r_s)/r_s$, $\hat{L}_s = L_s/r_s$, $L_s = R_0\,q_s/s_s$, $\hat{V}_E = V_E(r_s)/V_A$, $\hat{V}_* = V_*(r_s)/V_A$, $V_*(r) = (dp/dr)/(e\,n_0\,B_z)$ is the (dominant θ-component of the) diamagnetic velocity, and $\hat{V}_\parallel = \hat{d}_i\,V_z(r_s)/V_A$. Here, $s_s = s(r_s)$, and $s(r) = d\ln q/d\ln r$ is the magnetic shear. We also have

$$J(\hat{x}) = -\left(\frac{2}{s_s} - 1\right)\frac{1}{\hat{L}_s}, \tag{36}$$

and $\hat{E}_\parallel(\hat{x}) = (2/s_s - 1)\,(\hat{\eta}_\parallel/\hat{L}_s)$.

A.5 Derivation of linear layer equations

Suppose that the magnetic perturbation has m periods in the poloidal angle, and n periods in the toroidal angle. In accordance with Eqs. (32)–(36), let us write [21]

$$\psi(\hat{x}, \zeta) = \frac{\hat{x}^2}{2\,\hat{L}_s} + \tilde{\psi}(\hat{x})\,e^{i\zeta}, \tag{37}$$

$$\phi(\hat{x}, \zeta) = -\hat{V}_E\,\hat{x} + \tilde{\phi}(\hat{x})\,e^{i\zeta}, \tag{38}$$

$$N(\hat{x}, \zeta) = -\hat{V}_*\,\hat{x} + \iota_e\,\tilde{N}(\hat{x})\,e^{i\zeta}, \tag{39}$$

$$V(\hat{x}, \zeta) = \hat{V}_\parallel + \iota_e\,\tilde{V}(\hat{x})\,e^{i\zeta}, \tag{40}$$

$$J(\hat{x}, \zeta) = -\left(\frac{2}{s_s} - 1\right)\frac{1}{\hat{L}_s} + \hat{\nabla}^2\tilde{\psi}(\hat{x})\,e^{i\zeta}, \tag{41}$$

where $\zeta = m\,\theta - n\,\varphi$. Here, $\tilde{\ }$ denotes a perturbed quantity. Substituting Eqs. (37)–(41) into Eqs. (27)–(31), and only retaining terms that are first order in perturbed quantities, we obtain the following set of linear equations:

$$-i\,n\,(\omega_E + \omega_{*\,e})\,\tau_H\,\tilde{\psi} = -i\,\hat{x}\,(\tilde{\phi} - \tilde{N}) + S^{-1}\,\hat{\nabla}^2\tilde{\psi}, \tag{42}$$

$$-i\,n\,\omega_E\,\tau_H\,\tilde{N} = i\,n\,\omega_{*\,e}\,\tau_H\,\tilde{\phi} - i\,\iota_e\,\hat{d}_\beta^2\,\hat{x}\,\hat{\nabla}^2\tilde{\psi} - i\,c_\beta^2\,\hat{x}\,\tilde{V} + S^{-1}\,P_E\,\hat{\nabla}^2\tilde{N}, \tag{43}$$

$$-i\,n\,(\omega_E + \omega_{*\,i})\,\tau_H\,\hat{\nabla}^2\tilde{\phi} = -i\,\hat{x}\,\hat{\nabla}^2\tilde{\psi} + S^{-1}\,P_\varphi\,\hat{\nabla}^4\left(\tilde{\phi} + \frac{\tilde{N}}{\iota}\right), \tag{44}$$

$$-i\,n\,\omega_E\,\tau_H\,\tilde{V} = -i\,n\,\omega_{*\,e}\,\tau_H\,\tilde{\psi} - i\,\hat{x}\,\tilde{N} + S^{-1}\,P_\varphi\,\hat{\nabla}^2\tilde{V}. \tag{45}$$

Here, $\tau_H = L_s/[m\,V_A(r_s)]$ is the hydromagnetic time, $\omega_E = -(q_s/r_s)\,V_E(r_s) = -(d\Phi/d\psi_p)_{r_s}$ the $\mathbf{E} \times \mathbf{B}$ frequency, $\omega_{*e} = \iota_e\,(q_s/r_s)V_*(r_s) = [(dp_e/d\psi_p)/(e\,n_e)]_{r_s}$ the electron diamagnetic frequency, $\omega_{*i} = -\iota_i\,(m/r_s)V_*(r_s) = -[(dp_i/d\psi_p)/(e\,n_e)]_{r_s}$ the ion diamagnetic frequency, $\Phi(r)$ the equilibrium electrostatic potential, $S = \tau_R/\tau_H$ the Lundquist number, $\tau_R = (\mu_0\,r^2/\eta_\parallel)_{r_s}$ the resistive diffusion time, $\tau_E = (r^2/\chi_E)_{r_s}$ the energy confinement time, and $\tau_\varphi = (r^2/\chi_\varphi)_{r_s}$ the toroidal momentum confinement time. Furthermore, $P_E = \tau_R/\tau_E$ and $P_\varphi = \tau_R/\tau_\varphi$ are magnetic Prandtl numbers.

Let us define the stretched radial variable $X = S^{1/3}\,\hat{x}$. Assuming that $X \sim \mathcal{O}(1)$ in the layer (i.e., assuming that the layer thickness is roughly of order $S^{-1/3}\,r_s$), and making use of the fact that $S \gg 1$ in conventional tokamak plasmas, Eqs. (42)–(45) reduce to the following set of linear layer equations [14, 17]:

$$\mathrm{i}\,(Q_E + Q_e)\,\tilde{\psi} = -\mathrm{i}\,X\left(\tilde{\phi} - \tilde{N}\right) + \frac{d^2\tilde{\psi}}{dX^2}, \tag{46}$$

$$\mathrm{i}\,Q_E\,\tilde{N} = -\mathrm{i}\,Q_e\,\tilde{\phi} - \mathrm{i}\,D^2\,X\,\frac{d^2\tilde{\psi}}{dX^2} - \mathrm{i}\,c_\beta^2\,X\,\tilde{V} + P_E\,\frac{d^2\tilde{N}}{dX^2}, \tag{47}$$

$$\mathrm{i}\,(Q_E + Q_i)\,\frac{d^2\tilde{\phi}}{dX^2} = -\mathrm{i}\,X\,\frac{d^2\tilde{\psi}}{dX^2} + P_\varphi\,\frac{d^4}{dX^4}\left(\tilde{\phi} + \frac{\tilde{N}}{\iota}\right), \tag{48}$$

$$\mathrm{i}\,Q_E\,\tilde{V} = \mathrm{i}\,Q_e\,\tilde{\psi} - \mathrm{i}\,X\,\tilde{N} + P_\varphi\,\frac{d^2\tilde{V}}{dX^2}. \tag{49}$$

Here, $Q_E = -S^{1/3}\,n\,\omega_E\,\tau_H$, $Q_{e,i} = -S^{1/3}\,n\,\omega_{*\,e,i}\,\tau_H$, and $D = S^{1/3}\,\iota_e^{1/2}\,\hat{d}_\beta$.

If we write $P_E = c_\beta^2$ then Eqs. (46)–(49) become equivalent to the set of layer equations solved by Lee et alia. (To be slightly more exact, we get from our equations to those of Lee et alia by making the following transformation: $Q_E \to Q$, $Q_e \to -Q_{*\,e}$, $Q_i \to -Q_{*\,i}$, $\iota \to 1/\tau$, $P_E \to c_\beta^2$, $P_\varphi \to P$, $\tilde{\psi} \to -\tilde{\psi}$, $\tilde{N} \to \tilde{Z}$, $\tilde{\phi} \to \tilde{\phi}$, and $\tilde{V} \to -\tilde{V}_z$.)

The low-β approximation used in Refs. [14] and [17] involves neglecting the term containing c_β^2 in Eq. (47). This approximation decouples Eq. (49) from the three preceding equations, and effectively converts a four-field resonant response model into a three-field model. In the following, we shall not make use of this approximation.

A.6   Asymptotic matching

The linear layer equations, (46)–(49), possess tearing parity solutions characterized by the symmetry $\tilde{\psi}(-X) = \tilde{\psi}(X)$, $\tilde{N}(-X) = -\tilde{N}(X)$, $\tilde{\phi}(-X) = -\tilde{\phi}(X)$, $\tilde{V}(-X) = \tilde{V}(X)$. As is easily demonstrated, the asymptotic behavior of the tearing parity solution to Eqs. (46)–(49) is such that

$$\tilde{\psi}(X) \to \psi_0\left[\frac{\hat{\Delta}}{2}\,|X| + 1 + \mathcal{O}\left(\frac{1}{X^2}\right)\right], \tag{50}$$

$$\tilde{\phi}(X) \to -\psi_0\,Q_E\left[\frac{\hat{\Delta}}{2}\,\mathrm{sgn}(X) + \frac{1}{X} + \mathcal{O}\left(\frac{1}{X^2}\right)\right], \tag{51}$$

$$\tilde{N}(X) \to \psi_0\,Q_e\left[\frac{\hat{\Delta}}{2}\,\mathrm{sgn}(X) + \frac{1}{X} + \mathcal{O}\left(\frac{1}{X^2}\right)\right], \tag{52}$$

$$\tilde{V}(X) \to \mathcal{O}\left(\frac{1}{X^3}\right) \tag{53}$$

as $|X| \to \infty$, where ψ_0 is an arbitrary constant. It follows from Eq. (4) that layer response index is

$$\Delta_s = S^{1/3}\,\hat{\Delta}. \tag{54}$$

A.7   Fourier transformation

Equations (46)–(49) are most conveniently solved in Fourier transform space [14]. Let

$$\bar{\phi}(p) = \int_{-\infty}^{\infty} \tilde{\phi}(X)\,\mathrm{e}^{-\mathrm{i}\,p\,X}\,dX, \tag{55}$$

et cetera. The Fourier transformed linear layer equations become

$$\mathrm{i}\,(Q_E + Q_e)\,\bar{\psi} = \frac{d}{dp}\left(\bar{\phi} - \bar{N}\right) - p^2\,\bar{\psi}, \tag{56}$$

$$\mathrm{i}\,Q_E\,\bar{N} = -\mathrm{i}\,Q_e\,\bar{\phi} - D^2\,\frac{d(p^2\,\bar{\psi})}{dp} + c_\beta^2\,\frac{d\bar{V}}{dp} - P_E\,p^2\,\bar{N}, \tag{57}$$

$$\mathrm{i}\,(Q_E + Q_i)\,p^2\,\bar{\phi} = \frac{d(p^2\,\bar{\psi})}{dp} - P_\varphi\,p^4\left(\bar{\phi} + \frac{\bar{N}}{\iota}\right), \tag{58}$$

$$\mathrm{i}\,Q_E\,\bar{V} = \mathrm{i}\,Q_e\,\bar{\psi} + \frac{d\bar{N}}{dp} - P_\varphi\,p^2\,\bar{V}, \tag{59}$$

where, for a tearing parity solution,

$$\bar{\phi}(p) - \bar{N}(p) \equiv \bar{Y}(p) \to \bar{Y}_0\left[\frac{\hat{\Delta}}{\pi\,p} + 1 + \mathcal{O}(p)\right] \tag{60}$$

as $p \to 0$. Here, $\bar{Y}_0$ is an arbitrary constant.

Finally, if we define

$$\bar{J}(p) = p^2\,\bar{\psi}, \tag{61}$$

then Eqs. (56)–(59) can be converted into the following equivalent set of four, coupled, first-order o.d.e.s:

$$\frac{d\bar{Y}}{dp} = \left[\frac{\mathrm{i}\,(Q_E + Q_e) + p^2}{p^2}\right]\bar{J}, \tag{62}$$

$$\frac{d\bar{N}}{dp} = -\left(\frac{\mathrm{i}\,Q_e}{p^2}\right)\bar{J} + (\mathrm{i}\,Q_E + P_\varphi\,p^2)\,\bar{V}, \tag{63}$$

$$\frac{d\bar{J}}{dp} = [\mathrm{i}\,(Q_E + Q_i)\,p^2 + P_\varphi\,p^4]\,\bar{Y} + [\mathrm{i}\,(Q_E + Q_i)\,p^2 + \iota_e^{-1}\,P_\varphi\,p^4]\,\bar{N}, \tag{64}$$

$$c_\beta^2\,\frac{d\bar{V}}{dp} = [\mathrm{i}\,Q_e + \mathrm{i}\,(Q_E + Q_i)\,D^2\,p^2 + D^2\,P_\varphi\,p^4]\,\bar{Y}$$
$$+ \{\mathrm{i}\,(Q_E + Q_e) + [P_E + \mathrm{i}\,(Q_E + Q_i)\,D^2]\,p^2 + \iota_e^{-1}\,D^2\,P_\varphi\,p^4\}\,\bar{N}, \tag{65}$$

Note that $\iota_e = -Q_e/(Q_i - Q_e)$.

A.8 Small argument expansion

Let us search for power-law solutions of Eqs. (62)–(65) at small values of p. Given that we have four, coupled, first-order o.d.e.s, we expect to find four independent power-law solutions. The first solution is such that

$$\bar{Y}(p) = \mathrm{i}\,(Q_E + Q_e)\,a_{-1}\,p^{-1} - \left[\frac{\mathrm{i}}{2}\,Q_E\,(Q_E + Q_e)\,(Q_E + Q_i) + 1\right]a_{-1}\,p + \mathcal{O}(p^3), \tag{66}$$

$$\bar{N}(p) = -\mathrm{i}\,Q_e\,a_{-1}\,p^{-1} + \frac{\mathrm{i}}{2}\,Q_E\,Q_e\,(Q_E + Q_i)\,a_{-1}\,p + \mathcal{O}(p^3), \tag{67}$$

$$\bar{J}(p) = -a_{-1} - \frac{1}{2}\,Q_E\,(Q_E + Q_i)\,a_{-1}\,p^2 + \mathcal{O}(p^4), \tag{68}$$

$$\bar{V}(p) = -\frac{[\mathrm{i}\,Q_e\,(1 + P_E) + Q_E\,(Q_E + Q_i)\,D^2]}{2\,c_\beta^2}\,a_{-1}\,p^2 + \mathcal{O}(p^4), \tag{69}$$

where a_{-1} is an arbitrary constant. The second solution is such that

$$\bar{Y}(p) = \mathrm{i}\,(Q_E + Q_e)\,a_0 - \frac{\mathrm{i}}{6}\,Q_E\,(Q_E + Q_e)\,(Q_E + Q_i)\,a_0\,p^2 + \mathcal{O}(p^4), \tag{70}$$

$$\bar{N}(p) = -\mathrm{i}\,Q_e\,a_0 + \frac{\mathrm{i}}{6}\,Q_E\,Q_e\,(Q_E + Q_i)\,a_0\,p^2 + \mathcal{O}(p^4), \tag{71}$$

$$\bar{J}(p) = -\frac{1}{3}\,Q_E\,(Q_E + Q_i)\,a_0\,p^3 + \mathcal{O}(p^5), \tag{72}$$

$$\bar{V}(p) = -\frac{1}{3}\,\frac{[\mathrm{i}\,Q_e\,P_E + Q_E\,(Q_E + Q_i)\,D^{\,2}]}{c_\beta^2}\,a_0\,p^3 + \mathcal{O}(p^5), \tag{73}$$

where a_0 is an arbitrary constant. The third solution is such that

$$\bar{Y}(p) = -\frac{1}{6}\,(Q_E + Q_e)\,(Q_E + Q_i)\,a_2\,p^2 + \mathcal{O}(p^4), \tag{74}$$

$$\bar{N}(p) = a_2 + \frac{\mathrm{i}}{2}\,(Q_E + Q_i)\left(-\frac{\mathrm{i}}{3}\,Q_e + \frac{g}{c_\beta^2}\right)a_2\,p^2 + \mathcal{O}(p^4), \tag{75}$$

$$\bar{J}(p) = \frac{\mathrm{i}}{3}\,(Q_E + Q_i)\,a_2\,p^3 + \mathcal{O}(p^5), \tag{76}$$

$$\bar{V}(p) = \mathrm{i}\,\frac{(Q_E + Q_e)}{c_\beta^2}\,a_2\,p + \mathcal{O}(p^3), \tag{77}$$

where a_2 is an arbitrary constant. The final solution is such that

$$\bar{Y}(p) = -\frac{\mathrm{i}}{12}\,Q_E\,(Q_E + Q_e)\,(Q_E + Q_i)\,a_3\,p^3 + \mathcal{O}(p^5), \tag{78}$$

$$\bar{N}(p) = -\mathrm{i}\,Q_E\,a_3\,p + \mathcal{O}(p^3), \tag{79}$$

$$\bar{J}(p) = -\frac{1}{4}\,Q_E\,(Q_E + Q_i)\,a_3\,p^4 + \mathcal{O}(p^6), \tag{80}$$

$$\bar{V}(p) = -\frac{Q_E\,(Q_E + Q_e)}{2\,c_\beta^2}\,a_3\,p^2 + \mathcal{O}(p^4), \tag{81}$$

where a_3 is an arbitrary constant. Note, however, that the third solution is not consistent with Eqs. (50)–(53), which mandate that $\bar{N}(p) \to -[Q_e/(Q_E + Q_e)]\,\bar{Y}(p) + \mathcal{O}(p)$ and $\bar{V}(p) \to \mathcal{O}(p^2)$ as $p \to 0$. Hence, we deduce that $a_2 = 0$.

We conclude that, at small values of p, the most general solution for $\bar{Y}(p)$ and $\bar{N}(p)$ takes the form

$$\bar{Y}(p) = \mathrm{i}\,(Q_E + Q_e)\,(a_{-1}\,p^{-1} + a_0) + \mathcal{O}(p), \tag{82}$$

$$\bar{N}(p) = -\mathrm{i}\,Q_e\,(a_{-1}\,p^{-1} + a_0) + \mathcal{O}(p), \tag{83}$$

which is consistent with Eqs. (50)–(53).

A.9 Ricatti matrix differential equation

Let

$$\underline{u} = \begin{pmatrix} \bar{Y} \\ \bar{N} \end{pmatrix}, \tag{84}$$

$$\underline{v} = \begin{pmatrix} \bar{J} \\ c_\beta^2\,\bar{V} \end{pmatrix}. \tag{85}$$

Equations (62)–(65) can be written in the form

$$\frac{d\underline{u}}{dp} = \underline{\underline{A}}\,\underline{v}, \tag{86}$$

$$\frac{d\underline{v}}{dp} = \underline{\underline{B}}\,\underline{u}, \tag{87}$$

where

$$A_{11} = \frac{\mathrm{i}\,(Q_E + Q_e) + p^2}{p^2}, \tag{88}$$

$$A_{12} = 0, \tag{89}$$

$$A_{21} = -\frac{\mathrm{i}\,Q_e}{p^2}, \tag{90}$$

$$A_{22} = \frac{\mathrm{i}\,Q_E + P_\varphi\,p^2}{c_\beta^2}, \tag{91}$$

$$B_{11} = \mathrm{i}\,(Q_E + Q_i)\,p^2 + P_\varphi\,p^4, \tag{92}$$

$$B_{12} = \mathrm{i}\,(Q_E + Q_i)\,p^2 + \iota_e^{-1}\,P_\varphi\,p^4, \tag{93}$$

$$B_{21} = \mathrm{i}\,Q_e + \mathrm{i}\,(Q_E + Q_i)\,D^2\,p^2 + D^2\,P_\varphi\,p^4, \tag{94}$$

$$B_{22} = \mathrm{i}\,(Q_E + Q_e) + [P_E + \mathrm{i}\,(Q_E + Q_i)\,D^2]\,p^2 + \iota_e^{-1}\,D^2\,P_\varphi\,p^4. \tag{95}$$

Thus, we obtain the following matrix differential equation:

$$\frac{d}{dp}\left(\underline{\underline{A}}^{-1}\,\frac{d\underline{u}}{dp}\right) = \underline{\underline{B}}\,\underline{u}. \tag{96}$$

Let

$$p\,\frac{d\underline{u}}{dp} = \underline{\underline{W}}\,\underline{u}. \tag{97}$$

The previous two equations can be combined to give

$$\left(p\,\frac{d\underline{\underline{W}}}{dp} - \underline{\underline{W}} + \underline{\underline{W}}\,\underline{\underline{W}} + \underline{\underline{A}}\,p\,\frac{d\underline{\underline{A}}^{-1}}{dp}\,\underline{\underline{W}} - p^2\,\underline{\underline{A}}\,\underline{\underline{B}}\right)\underline{u} = \underline{0}, \tag{98}$$

which yields the Riccati matrix differential equation,

$$p\,\frac{d\underline{\underline{W}}}{dp} = \underline{\underline{W}} - \underline{\underline{W}}\,\underline{\underline{W}} - \underline{\underline{E}}\,\underline{\underline{W}} + \underline{\underline{F}}, \tag{99}$$

where

$$\underline{\underline{E}}(p) = \underline{\underline{A}}\,p\,\frac{d\underline{\underline{A}}^{-1}}{dp}, \tag{100}$$

$$\underline{\underline{F}}(p) = p^2\,\underline{\underline{A}}\,\underline{\underline{B}}. \tag{101}$$

In fact, it is easily demonstrated that

$$E_{11} = \frac{2\,\mathrm{i}\,(Q_E + Q_e)}{\mathrm{i}\,(Q_E + Q_e) + p^2}, \tag{102}$$

$$E_{12} = 0, \tag{103}$$

$$E_{21} = -\frac{2\,\mathrm{i}\,Q_e\,(\mathrm{i}\,Q_E + 2\,P_\varphi\,p^2)}{[\mathrm{i}\,(Q_E + Q_e) + p^2]\,(\mathrm{i}\,Q_E + P_\varphi\,p^2)}, \tag{104}$$

$$E_{22} = -\frac{2\,P_\varphi\,p^2}{\mathrm{i}\,Q_E + P_\varphi\,p^2}, \tag{105}$$

and

$$F_{11} = p^2\,[\mathrm{i}\,(Q_E + Q_e) + p^2]\,[\mathrm{i}\,(Q_E + Q_i) + P_\varphi\,p^2], \tag{106}$$

$$F_{12} = p^2\,[\mathrm{i}\,(Q_E + Q_e) + p^2]\,[\mathrm{i}\,(Q_E + Q_i) + \iota_e^{-1}\,P_\varphi\,p^2], \tag{107}$$

$$F_{21} = -\mathrm{i}\,Q_e\,p^2\,[\mathrm{i}\,(Q_E + Q_i) + P_\varphi\,p^2]$$
$$\qquad + c_\beta^{-2}\,p^2\,(\mathrm{i}\,Q_E + P_\varphi\,p^2)\,[\mathrm{i}\,Q_e + \mathrm{i}\,(Q_E + Q_i)\,D^2\,p^2 + D^2\,P_\varphi\,p^4], \tag{108}$$

$$F_{22} = -\mathrm{i}\,Q_e\,p^2\,[\mathrm{i}\,(Q_E + Q_i) + \iota_e^{-1}\,P_\varphi\,p^2]$$
$$\qquad + c_\beta^{-2}\,p^2\,(\mathrm{i}\,Q_E + P_\varphi\,p^2)\,\{\mathrm{i}\,(Q_E + Q_e) + [P_E + \mathrm{i}\,(Q_E + Q_i)\,D^2]\,p^2 + \iota_e^{-1}\,D^2\,P_\varphi\,p^4\}. \tag{109}$$

Finally, if

$$\underline{\underline{W}}(p) = \begin{pmatrix} W_{11}, & W_{12} \\ W_{21}, & W_{22} \end{pmatrix} \tag{110}$$

then Eq. (99) yields

$$p\,\frac{dW_{11}}{dp} = W_{11} - W_{11}\,W_{11} - W_{12}\,W_{21} - E_{11}\,W_{11} + F_{11}, \tag{111}$$

$$p\,\frac{dW_{12}}{dp} = W_{12} - W_{11}\,W_{12} - W_{12}\,W_{22} - E_{11}\,W_{12} + F_{12}, \tag{112}$$

$$p\,\frac{dW_{21}}{dp} = W_{21} - W_{21}\,W_{11} - W_{22}\,W_{21} - E_{21}\,W_{11} - E_{22}\,W_{21} + F_{21}, \tag{113}$$

$$p\,\frac{dW_{22}}{dp} = W_{22} - W_{21}\,W_{12} - W_{22}\,W_{22} - E_{21}\,W_{12} - E_{22}\,W_{22} + F_{22}. \tag{114}$$

Thus, our final system of equations consists of a set of four, coupled, nonlinear differential equations.

A.10 Small-argument behavior of Riccati matrix differential equation

It follows from Eqs. (102)–(105) that $\underline{\underline{E}}(p) = \underline{\underline{E}}^{\,(0)} + \mathcal{O}(p^2)$ at small values of p, where

$$E_{11}^{(0)} = 2, \tag{115}$$

$$E_{12}^{(0)} = 0, \tag{116}$$

$$E_{21}^{(0)} = -\frac{2\,Q_e}{Q_E + Q_e}, \tag{117}$$

$$E_{22}^{(0)} = 0. \tag{118}$$

Likewise, Eqs. (106)–(109) imply that $\underline{\underline{F}}(p) = \mathcal{O}(p^2)$.

Suppose that $\underline{\underline{W}}(p) = \underline{\underline{W}}^{(0)} + \underline{\underline{W}}^{(1)} p$ at small values of p, where the elements of $\underline{\underline{W}}^{(0)}$ and $\underline{\underline{W}}^{(1)}$ are independent of p. Equation (99) gives

$$\underline{\underline{0}} = \underline{\underline{W}}^{(0)} - \underline{\underline{W}}^{(0)} \underline{\underline{W}}^{(0)} - \underline{\underline{E}}^{(0)} \underline{\underline{W}}^{(0)}, \tag{119}$$

$$\underline{\underline{0}} = -\underline{\underline{W}}^{(1)} \underline{\underline{W}}^{(0)} - \underline{\underline{W}}^{(0)} \underline{\underline{W}}^{(1)} - \underline{\underline{E}}^{(0)} \underline{\underline{W}}^{(1)}. \tag{120}$$

Suitable solutions are

$$\underline{\underline{W}}^{(0)} = \begin{pmatrix} -1, & 0 \\ -E_{21}^{(0)}/2, & 0 \end{pmatrix}, \tag{121}$$

$$W_{12}^{(1)} = 0, \tag{122}$$

$$W_{21}^{(1)} = \frac{E_{21}^{(0)}}{2} \left[W_{11}^{(1)} - W_{22}^{(1)} \right]. \tag{123}$$

At small values of p, let

$$\underline{u}(p) = \underline{u}_{-1} \, p^{-1} + \underline{u}_0, \tag{124}$$

where the elements of $\underline{u}_{-1}$ (which are y_{-1} and n_{-1}, respectively) and the elements of $\underline{u}_0$ (which are y_0 and n_0, respectively) are all constants. Equation (97) gives

$$\underline{\underline{W}}^{(0)} \, \underline{u}_{-1} = -\underline{u}_{-1}, \tag{125}$$

$$\underline{\underline{W}}^{(0)} \, \underline{u}_0 + \underline{\underline{W}}^{(1)} \, \underline{u}_{-1} = \underline{0}. \tag{126}$$

Thus, making use of Eq. (121), we get

$$\begin{pmatrix} -1, & 0 \\ -E_{21}^{(0)}/2, & 0 \end{pmatrix} \begin{pmatrix} y_{-1} \\ n_{-1} \end{pmatrix} = - \begin{pmatrix} y_{-1} \\ n_{-1} \end{pmatrix}, \tag{127}$$

which implies that

$$\frac{E_{21}^{(0)}}{2} \, y_{-1} = -\frac{Q_e}{Q_E + Q_e} \, y_{-1} = n_{-1}, \tag{128}$$

in accordance with Eqs. (82) and (83), where use has been made of Eq. (117). Equations (121)–(123) and (126) yield

$$\frac{y_0}{y_{-1}} = W_{11}^{(1)}, \tag{129}$$

with n_0 undetermined. It follows from Equation (60) that

$$\frac{\pi}{\hat{\Delta}} \equiv \frac{y_0}{y_{-1}} = W_{11}^{(1)} = \frac{dW_{11}(0)}{dp}. \tag{130}$$

Note, incidentally, that the result $\pi/\hat{\Delta} = y_0/y_{-1}$ follows directly from Eq. (46), and would hold even if a_2 were non-zero.

A.11 Large-argument behavior of Riccati matrix differential equation

At large values of p, it is clear from Eqs. (106)–(109) that $\underline{\underline{F}}(p) = \underline{\underline{F}}^{(6)} p^6 + \underline{\underline{F}}^{(8)} p^8$, where the elements of $\underline{\underline{F}}^{(6)}$ and $\underline{\underline{F}}^{(8)}$ are independent ot p. On the other hand, Eqs. (102)–(105) imply that $\underline{\underline{E}}(p) = \underline{\underline{E}}^{(0)}$, where

the elements of $\underline{\underline{E}}^{(0)}$ are independent of p. Thus, if we write $\underline{\underline{W}}(p) = \underline{\underline{W}}^{(2)}\, p^2 + \underline{\underline{W}}^{(4)}\, p^4$, where the elements of $\underline{\underline{W}}^{(2)}$ and $\underline{\underline{W}}^{(4)}$ are independent of p, then Eq. (99) gives

$$\underline{\underline{W}}^{(4)}\, \underline{\underline{W}}^{(4)} = \underline{\underline{F}}^{(8)}, \tag{131}$$

$$\underline{\underline{W}}^{(2)}\, \underline{\underline{W}}^{(4)} + \underline{\underline{W}}^{(4)}\, \underline{\underline{W}}^{(2)} = \underline{\underline{F}}^{(6)}. \tag{132}$$

Now, according to Eqs. (106)–(109),

$$F_{11}^{(8)} = 0, \tag{133}$$

$$F_{12}^{(8)} = 0, \tag{134}$$

$$F_{21}^{(8)} = c_\beta^{-2}\, D^2\, P_\varphi^2, \tag{135}$$

$$F_{22}^{(8)} = c_\beta^{-2}\, \iota_e^{-1}\, D^2\, P_\varphi^2, \tag{136}$$

so Eq. (131) yields

$$W_{11}^{(4)} = 0, \tag{137}$$

$$W_{12}^{(4)} = 0, \tag{138}$$

$$W_{21}^{(4)} = -c_\beta^{-1}\, \iota_e^{1/2}\, D\, P_\varphi, \tag{139}$$

$$W_{22}^{(4)} = -c_\beta^{-1}\, \iota_e^{-1/2}\, D\, P_\varphi, \tag{140}$$

where we have chosen the sign of the square root that is associated with well-behaved solutions at large values of p. Here, we are assuming that $\iota_e > 0$. Equations (106)–(109) also give

$$F_{11}^{(6)} = P_\varphi, \tag{141}$$

$$F_{12}^{(6)} = \iota_e^{-1}\, P_\varphi, \tag{142}$$

$$F_{21}^{(6)} = \mathrm{i}\, c_\beta^{-2}\, Q_E\, D^2\, P_\varphi + \mathrm{i}\, c_\beta^{-2}\, (Q_E + Q_i)\, D^2\, P_\varphi, \tag{143}$$

$$F_{22}^{(6)} = \mathrm{i}\, c_\beta^{-2}\, \iota_e^{-1}\, Q_E\, D^2\, P_\varphi + c_\beta^{-2}\, [P_E + \mathrm{i}\, (Q_E + Q_i)\, D^2]\, P_\varphi. \tag{144}$$

Thus, Eq. (132) yields

$$W_{12}^{(2)}\, W_{21}^{(4)} = F_{11}^{(6)}, \tag{145}$$

$$W_{12}^{(2)}\, W_{22}^{(4)} = F_{12}^{(6)}, \tag{146}$$

which gives

$$W_{12}^{(2)} = -c_\beta\, \iota_e^{-1/2}\, D^{-1}. \tag{147}$$

Now, if

$$\underline{\underline{W}}\, \underline{u} = \lambda(p)\, \underline{u} \tag{148}$$

then Eq. (97) yields

$$p\, \frac{d\underline{u}}{dp} = \lambda\, \underline{u}, \tag{149}$$

which implies that

$$\underline{u}(p) = \underline{u}(p_0)\, \exp\left[\int_{p_0}^{p} \frac{\lambda_r(p')}{p'}\, dp'\right] \exp\left[\mathrm{i} \int_{p_0}^{p} \frac{\lambda_i(p')}{p'}\, dp'\right], \tag{150}$$

27

where λ_r and λ_i are the real and imaginary parts of λ, respectively. Of course, a solution that is well behaved at large values of p is such that λ_r is negative. As we have seen, the large-p limit of Eq. (99) is

$$\underline{\underline{W}}\,\underline{\underline{W}} = \underline{\underline{F}}. \tag{151}$$

Hence, if

$$\underline{\underline{F}}\,\underline{u} = \Lambda\,\underline{u} \tag{152}$$

then Eqs. (148) and (152) imply that

$$\lambda^2 = \Lambda. \tag{153}$$

The eigenvalue problem for the F-matrix reduces to

$$\Lambda^2 - (F_{11} + F_{22})\,\Lambda + F_{11}\,F_{22} - F_{12}\,F_{21} = 0. \tag{154}$$

Now,

$$F_{11} + F_{22} \simeq F_{22}^{(8)}\,p^8 = c_\beta^{-2}\,\iota_e^{-1}\,D^2\,P_\varphi^2\,p^8, \tag{155}$$

$$F_{11}\,F_{22} - F_{12}\,F_{21} \simeq \left[F_{11}^{(6)}\,F_{22}^{(8)} - F_{12}^{(6)}\,F_{21}^{(8)} \right] p^{14}$$

$$+ \left[F_{11}^{(6)}\,F_{22}^{(6)} - F_{12}^{(6)}\,F_{21}^{(6)} \right] p^{12} = c_\beta^{-2}\,R\,P_\varphi^2\,p^{12}, \tag{156}$$

where

$$R = P_E + \mathrm{i}\,(1 - \iota_e^{-1})\,(Q_E + Q_i)\,D^2, \tag{157}$$

Hence, the two eigenvalues of the F-matrix are

$$\Lambda_1 \simeq F_{22}^{(8)}\,p^8 = c_\beta^{-2}\,\iota_e^{-1}\,D^2\,P_\varphi^2\,p^8, \tag{158}$$

$$\Lambda_2 \simeq \frac{[F_{11}^{(6)}\,F_{22}^{(6)} - F_{12}^{(6)}\,F_{21}^{(6)}]}{F_{22}^{(8)}}\,p^4 = \iota_e\,D^{-2}\,R\,p^4. \tag{159}$$

Thus, we deduce that the two eigenvalues of the W-matrix are

$$\lambda_1 = -\Lambda_1^{1/2} = -c_\beta^{-1}\,\iota_e^{-1/2}\,D\,P_\varphi\,p^4, \tag{160}$$

$$\lambda_2 = -\Lambda_2^{1/2} = -\iota_e^{1/2}\,D^{-1}\,R^{1/2}\,p^2, \tag{161}$$

Here, the square root of R is taken such that the real part of λ_2 is negative. Now, the eigenvalue problem for the W-matrix reduces to

$$\lambda^2 - W_{22}^{(4)}\,p^4\,\lambda + \left[W_{11}^{(2)}\,W_{22}^{(4)} - W_{12}^{(2)}\,W_{21}^{(4)} \right] p^6 = 0. \tag{162}$$

which yields

$$\lambda_1 \simeq W_{22}^{(4)}\,p^4, \tag{163}$$

which is in agreement with Eq. (160), and

$$\lambda_2 \simeq \left[W_{11}^{(2)} - \frac{W_{12}^{(2)}\,W_{21}^{(4)}}{W_{22}^{(4)}} \right] p^2, \tag{164}$$

which implies that

$$W_{11}^{(2)} = -\iota_e^{1/2}\,D^{-1}\,R^{1/2} - c_\beta\,\iota_e^{1/2}\,D^{-1}. \tag{165}$$

Hence, the large-p boundary condition for the W-matrix is

$$\underline{\underline{W}}(p) = \begin{pmatrix} -\iota_e^{1/2}\,D^{-1}\,R^{1/2}\,p^2 - c_\beta\,\iota_e^{1/2}\,D^{-1}\,p^2, & -c_\beta\,\iota_e^{-1/2}\,D^{-1}\,p^2 \\ -c_\beta^{-1}\,\iota_e^{1/2}\,D\,P_\varphi\,p^4, & -c_\beta^{-1}\,\iota_e^{-1/2}\,D\,P_\varphi\,p^4 \end{pmatrix}. \tag{166}$$

A.12 Method of solution

The method of solution is to launch the well-behaved asymptotic solution (166) of Eqs. (111)–(114) from large p, and then integrate the equations backward to small p. The scaled layer response index, $\hat{\Delta}$, is then determined from Eq. (130). Note that, because there are no free parameters in expression (166), the scaled layer response index is uniquely determined by this procedure. Finally, the true layer response index is given by $\Delta_s = S^{1/3}\,\hat{\Delta}$. [See Eq. (54).]

References

[1] J.T. Scoville, R.J. La Haye, A.G. Kellman, T.H. Osborne, R.D. Stambaugh, E.J. Strait and T.S. Taylor, *Locked modes in DIII-D and a method for prevention of the low density mode*, Nucl. Fusion **31**, 875 (1991).

[2] T.C. Hender, R. Fitzpatrick, A.W. Morris, P.G. Carolan, R.D. Durst, T. Edlington, J. Ferreira, S.J. Fielding, P.S. Haynes, J. Hugill, et al., *Effect of resonant magnetic perturbations on COMPASS-C tokamak discharges*, Nucl. Fusion **32**, 2091 (1992).

[3] G.M. Fishpool and P.S. Haynes, *Field error instabilities in JET*, Nucl. Fusion **34**, 109 (1994).

[4] R. Fitzpatrick, *Interaction of tearing modes with external structures in cylindrical geometry (plasma)*, Nucl. Fusion **33**, 1049 (1993).

[5] R. Fitzpatrick, *Bifurcated states of a rotating tokamak plasma in the presence of a static error-field*, Phys. Plasmas **5**, 3325 (1998).

[6] M. Pharr, N.C. Logan, C. Paz-Soldan, J.-K. Park and C. Hansen, *Error field predictability and consequences for ITER*, Nucl. Fusion **64**, 126025 (2024).

[7] T.E. Evans, R.A. Moyer, J.G. Watkins, P.R. Thomas, T.H. Osborne, J.A. Boedo, M.E. Fenstermacher, K.H. Finken, R.J. Groebner, M. Groth, et al., *Suppression of large edge-localized modes in high-confinement DIII-D plasmas with a stochastic magnetic boundary*, Phys. Rev. Lett. **92**, 235003 (2004).

[8] A.H. Boozer, *Physics of magnetically confined plasmas*, Rev. Mod. Phys. **76**, 1071 (2004).

[9] Z. Chang and J.D. Callen, *Global energy confinement degradation due to macroscopic phenomena in tokamaks*, Nucl. Fusion **30**, 219 (1990).

[10] H.P. Furth, J. Killeen and M.N. Rosenbluth, *Finite-resistivity instabilities of a sheet pinch*, Phys. Fluids **6**, 459 (1963).

[11] G. Ara, B. Basu, B. Coppi, G. Laval, M.N. Rosenbluth and B.V. Waddell, *Magnetic reconnection and $m = 1$ oscillations in current carrying plasmas*, Ann. Phys. (NY) **112**, 443 (1978).

[12] J.F. Drake and Y.C. Lee, *Kinetic theory of tearing instabilities*, Phys. Fluids **20**, 1341 (1977).

[13] F.L. Waelbroeck, *Shielding of resonant magnetic perturbations in the long mean-free-path regime*, Phys. Plasmas **10**, 4040 (2003).

[14] A. Cole and R. Fitzpatrick, *Drift-magnetohydrodynamical model of error-field penetration in tokamak plasmas*, Phys. Plasmas **13**, 032503 (2006).

[15] R. Fitzpatrick and F.L. Waelbroeck, *Two-fluid magnetic island dynamics in slab geometry. I. Isolated islands*, Phys. Plasmas **12**, 022307 (2005).

[16] R.D. Hazeltine, M. Kotschenreuther and P.G. Morrison, *A four-field model for tokamak plasma dynamics*, Phys. Fluids **28**, 2466 (1985).

[17] R. Fitzpatrick, *Influence of anomalous perpendicular transport on linear tearing mode dynamics in tokamak plasmas*, Phys. Plasmas **29**, 032507 (2022).

[18] Y. Lee, J.-K. Park and Y.-S. Na, *Effect of parallel flow on resonant layer responses in high beta plasmas*, Nucl. Fusion **64**, 106058 (2024).

[19] D.P. Brennan, A.J. Cole, C. Akcay and J.M. Finn, *Two fluid stability of rotating tokamak plasmas using machine learning*, Bul. Am. Phys. Soc. **64**, 249 (2019).

[20] J.-K. Park, *Parametric dependencies of resonant layer responses across linear, two-fluid, drift-MHD regimes*, Phys. Plasmas **29**, 072506 (2022).

[21] R. Fitzpatrick, *Tearing mode dynamics in tokamak plasmas*, (IOP Publishing, Bristol UK, 2023).

[22] H.R. Koslowski, Y. Liang, A. Krämer-Flecken, K. Löwenbrück, M. Von Hellermann, E. Westerhof, R.C. Wolf, O. Zimmermann, TEXTOR team, *Dependence of the threshold for perturbation field generated m/n= 2/1 tearing modes on the plasma fluid rotation*, Nucl. Fusion, **46**, L1 (2006).

[23] M.F.M De Bock, I.G.J. Classen, C. Busch, R.J.E. Jaspers, H.R. Koslowski, B. Unterberg, TEXTOR Team, *The interaction between plasma rotation, stochastic fields and tearing mode excitation by external perturbation fields*, Nucl. Fusion, **48**, 015007 (2008).

[24] C. Paz-Soldan, R. Nazikian, L. Cui, B.C. Lyons, D.M. Orlov, A. Kirk, N.C. Logan, T.H. Osborne, W. Suttrop and D.B. Weisberg, *The effect of plasma shape and neutral beam mix on the rotation threshold for RMP-ELM suppression*, Nucl. Fusion **59**, 056012 (2019).

[25] R. Fitzpatrick, *Response of a magnetically diverted tokamak plasma to a resonant magnetic perturbation*, arXiv 2511.07666 (2025).

[26] H.P. Furth, P.H. Rutherford and H. Selberg, *Tearing mode in the cylindrical tokamak*, Phys. Fluids **16**, 1054 (1973).

[27] J.A. Wesson, *Hydromagnetic stability of tokamaks*, Nucl. Fusion **18**, 87 (1978).

[28] R. Fitzpatrick, *Calculation of tearing mode stability in an inverse aspect-ratio expanded tokamak plasma equilibrium*, Phys. Plasmas **31**, 102507 (2024).

[29] R. Fitzpatrick, *Investigation of tearing mode stability near ideal stability boundaries via asymptotic matching techniques*, Phys. Plasmas **32**, 062509 (2025).

[30] F. Wagner, G. Becker, K. Behringer, D. Campbell, A. Eberhagen, W. Engelhardt, G. Fussmann, O. Gehre, J. Gernhardt, et al., *Regime of improved confinement and high beta in neutral-beam-heated divertor discharges of the ASDEX tokamak*, Phys. Rev. Lett. **49**, 1408 (1982).

[31] P.B. Snyder, H.R. Wilson, J.R. Ferron, L.L. Lao, A.W. Leonard, T.H. Osborne, A.D. Turnbull, D. Mossessian, M. Murakami and X.Q. Xu, *Edge localized modes and the pedestal: A model based on coupled peeling–ballooning modes*, Phys. Plasmas **9**, 2037 (2002).

[32] H. Zohm, *Edge localized modes (ELMs)*, Plasma Phys. Controlled Fusion **38**, 105 (1996).

[33] A. Loarte, G. Saibene, R. Sartori, M. Bécoulet, L. Horton, T. Eich, A. Herrmann, M. Laux, G. Matthews, S. Jachmich, et al., *ELM energy and particle losses and their extrapolation to burning plasma experiments*, J. Nucl. Mater. **313**, 962 (2003).

[34] Y. Liang, H.R. Koslowski, P.R. Thomas, E. Nardon, B. Alper, P. Andrew, Y. Andrew, G. Arnoux, Y. Baranov, M. Bécoulet, et al., *Active control of type-I edge-localized modes with perturbation fields in the JET tokamak*, Phys. Rev. Lett. **98**, 265004 (2007).

[35] W. Suttrop, T. Eich, J.C. Fuchs, S. Günter, A. Janzer, A. Herrmann, A. Kallenbach, P.T. Lang, T. Lunt, M. Maraschek, et al., *First observation of edge localized modes mitigation with resonant and nonresonant magnetic perturbations in ASDEX-Upgrade*, Phys. Rev. Lett. **106**, 225004 (2011).

[36] Y.M. Jeon, J.-K. Park, S.W. Yoon, W.H. Ko, S.G. Lee, K.D. Lee, G.S. Yun, Y.U. Nam, W.C. Kim, J.-G. Kwak, K.S. Lee, H.K. Kim, H.L. Yang, et al., *Suppression of edge localized modes in high-confinement KSTAR plasmas by nonaxisymmetric magnetic perturbations*, Phys. Rev. Lett. **109**, 035004 (2012).

[37] A. Kirk, I.T. Chapman, Y. Liu, P. Cahyna, P. Denner, G. Fishpool, C.J. Ham, J.R. Harrison, Y. Liang, E. Nardon, S. Saarelma, R. Scannell, A.J. Thornton, and MAST Team, *Understanding edge-localized mode mitigation by resonant magnetic perturbations on MAST*, Nucl. Fusion **53**, 043007 (2013).

[38] T. Sun, Y. Liang, Y.Q. Liu, S. Gu, X. Yang, W. Guo, T. Shi, M. Jia, L. Wang, B. Lyu, et al., *Nonlinear transition from mitigation to suppression of the edge localized mode with resonant magnetic perturbations in the EAST tokamak*, Phys. Rev. Lett. **117**, 115001 (2016).

[39] D.A. Ryan, C. Ham, A. Kirk, T. Markovic, S. Munaretto, L. Piron, S. Saarelma, W. Suttrop, A.J. Thornton, E. Viezzer, M. Willensdorfer, the MAST Upgrade Team and the EUROfusion Tokamak Exploitation Team, *First observation of RMP ELM mitigation on MAST Upgrade*, Plasma Phys. Control. Fusion **66**, 105003 (2024).

[40] Q.M. Hu, R. Nazikian, B.A. Grierson, N.C. Logan, J.-K. Park, C. Paz-Soldan and Q. Yu, *The density dependence of edge-localized-mode suppression and density pump-out by resonant magnetic perturbations in the DIII-D tokamak*, Phys. Plasmas **26**, 120702 (2019).

[41] Q.M. Hu, R. Nazikian, B.A. Grierson, N.C. Logan, C. Paz-Solden and Q. Yu, *The role of edge resonant magnetic perturbations in edge-localized-mode suppression and density pump-out in low-collisionality DIII-D plasmas*, Nucl. Fusion **60**, 076001 (2020).

[42] Q.M. Hu, R. Nazikian, B.A. Grierson, N.C. Logan, D.M. Orlav, C. Paz-Solden and Q. Yu, *Wide operational windows of edge-localized mode suppression by resonant magnetic perturbations in the DIII-D tokamak*, Phys. Rev. Lett. **125**, 045001 (2020).

[43] R. Fitzpatrick, *Theory of edge localized mode suppression by static resonant perturbations in the DIII-D tokamak*, Phys. Plasmas **27**, 042506 (2020).

[44] R. Fitzpatrick and A.O. Nelson, *An improved theory of the response of DIII-D H-mode discharges to static resonant magnetic perturbations and its implications for the suppression of edge localized modes*, Phys. Plasmas **27**, 072501 (2020).

[45] R.J. Bickerton, J.W. Connor and J.B. Taylor, *Diffusion driven plasma currents and bootstrap tokamak*, Nat. Phys. Sci. **229**, 110 (1971).

[46] R. Fitzpatrick, Phys. Plasmas **31**, *Inverse aspect-ratio expanded tokamak equilibria*, 082505 (2024).

[47] R.J. Groebner and S. Saarelma, *Elements of H-mode pedestal structure*, Plasma Phys. Control. Fusion **65**, 073001 (2023).

[48] X. Lin, Q.Q. Yang, G.S. Xu, G.Z. Jia, C. Zhang, Y.F. Wang, N.M. Li, N. Yan, R. Chen, X.Q. Xu, et al., *Edge-localized mode mitigation enabled by active control of pedestal density gradient with new EAST tokamak divertor*, Phys. Plasmas **32**, 012503 (2025).

[49] Q. Yu, S. Günter, and B.D. Scott, *Numerical modeling of linear drift-tearing mode stability*, Phys. Plasmas **10**, 797 (2003).

[50] Q. Yu and S. Günter, *Plasma response to externally applied resonant perturbations*, Nucl. Fusion **51**, 073030 (2011).

[51] C. Chrystal, B.A. Grierson, S.R. Haskey, A.C. Sontag, F.M. Poli, M.W. Shafer and J.S. de Grassie, *Predicting the rotation profile in ITER*, Nucl. Fusion **60**, 036003 (2020).

[52] Z.S. Hartwig and Y.A. Podpaly, *Magnetic fusion energy formulary*, (Massachusetts Institute of Technology, Cambridge MA, 2011).

[53] F.L. Hinton and C. Oberman, *Electrical conductivity of plasma in a spatially homogeneous magnetic field*, Nucl. Fusion **9**, 319 (1969).

[54] J.A. Wesson, *Tokamaks*, 4th ed., (Oxford University Press, Oxford UK, 2011).

[55] R.D. Hazeltine and J.D. Meiss, *Plasma confinement*, (Dover, New York NY, 2003).